



1 **Measurement Report: Comparative Analysis of Fluorescing African Dust Particles in Spain**
2 **and Puerto Rico**

3
4 Bighnaraj Sarangi¹, Darrel Baumgardner², Ana Isabel Calvo³, Benjamin Bolaños-Rosero⁴, Roberto
5 Fraile³, Alberto Rodríguez-Fernández⁵, Delia Fernández-González⁵, Carlos Blanco-Alegre³, Cátia
6 Gonçalves³, Estela D. Vicente³, Olga L. Mayol Bracero^{1,6}

7
8 ¹*Department of Environmental Sciences, University of Puerto Rico – Río Piedras Campus, San Juan, Puerto Rico, USA*

9 ²*Droplet Measurement Technologies, LLC, Longmont, Colorado, USA*

10 ³*Department of Physics, Universidad de León, 24071 León, Spain*

11 ⁴*Department of Microbiology and Medical Zoology, School of Medicine, University of Puerto Rico –Medical Sciences*
12 *Campus, San Juan, Puerto Rico, USA*

13 ⁵*Department of Biodiversity and Environmental Management, University of León, Spain*

14 ⁶*Now at Environment and Climate Sciences Department, Brookhaven National Laboratory, Upton, New York, USA*

15
16 Correspondence: Bighnaraj Sarangi (bighnarajsarangi1986@gmail.com)
17

18



19
20

Abstract

21 Measurements during episodes of African dust, made with two Wideband Integrated Bioaerosol
22 Spectrometers (WIBS), one on the northeastern coast of Puerto Rico and the other in the city of León,
23 Spain, show unmistakable, bioaerosol-like fluorescing aerosol particles (FAP) that can be associated
24 with these dust episodes. The Puerto Rico events occurred during a major incursion of African dust
25 during June 2020. The León events occurred in the late winter and spring of 2022 when widespread,
26 elevated layers of dust inundated the Iberian Peninsula. Satellite and back trajectory analyses confirm
27 that dust from Northern Africa was the source of the particles during both events. The WIBS measures
28 the size of individual particles in the range from 0.5 μm to 30 μm , derives a shape factor and classifies
29 seven types of fluorescence from the FAP. In general it is not possible to directly determine the
30 specific biological identity from fluorescence signatures, however, measurements of these types of
31 bioaerosols in laboratory studies allow us to compare ambient fluorescence patterns with whole
32 microbial cells measured under controlled conditions. Here we introduce some new metrics that offer
33 a more quantitative approach for comparing FAP characteristics derived from particles measured
34 under different environmental conditions. The analysis highlights the similarities and differences at
35 the two locations and reveals differences that can be attributed to the age and history of the dust
36 plumes, e.g., the amount of time that the air masses were in the mixed layer and the frequency of
37 precipitation along the air mass trajectory.

38
39
40 Keywords: African Dust, Bioaerosols, Fluorescing Aerosol Particles, WIBS, fluorescing particle
41 finger prints.

42



43 1.0 Introduction

44

45 Fungal spores, spread by air currents, are some of the most abundant components of the bioaerosol
46 population (Després et al., 2012). Their presence in the atmosphere has been linked to the formation
47 of cloud condensation and ice nuclei (CCN and IN), thus playing a key role in the hydrological cycle
48 (Huffman et al., 2013; Woo et al., 2018; Lawler et al., 2020). However, they also may have a negative
49 environmental impact as many of them are described as important phytopathogens and constitute a
50 hazard to animal and human health (Fröhlich-Nowoisky et al., 2016). Although there is a large fungal
51 biodiversity the most abundant taxa are Ascomycetes and Basidiomycetes (Fröhlich-Nowoisky et al.,
52 2009; Dietzel et al., 2019). The airborne spore load varies depending on the location and the season
53 since such loading is closely linked to the vegetation and the meteorological conditions (Kasprzyk
54 et al., 2015; Grinn-Gofroń et al., 2019; Anees-Hill et al., 2022; Rodríguez-Fernández et al., 2023).
55 Nevertheless, the annual airborne dynamics can be altered by extreme weather phenomena such as
56 thunderstorms, frontal systems or dust intrusions (Wu et al., 2004; Pulimood et al., 2007).

57

58 Dust intrusions are especially important because these long-distance, spore transport events allow
59 them to colonize new environments (Rodríguez-Arias et al., 2023). In fact, some of these African
60 dust (AD) events have been related to important environmental hazards such as decline of Caribbean
61 coral reefs (Shinn et al., 2000; Hallegraeff et al., 2014). Agglomeration processes may also occur
62 during these dust events, facilitating the adhesion of particulates with small diameters (40-90 nm)
63 onto the surfaces of the pollen grains and spores. Gravitational coagulation has been identified as the
64 most likely mechanism of deposition on particle surfaces of about 20 μm (pollen grains) during long
65 distance transport (Choël et al., 2022); however, other mechanisms of particle scavenging should not
66 be underestimated. Fungal spores typically carry an electrostatic charge due to the complex chemical
67 composition of their cell walls (Hannan, 1961; Leach, 1976; Feofilova, 2010; Wargenau et al., 2011).
68 The differences in electrostatic charges can cause other particles to bind to the spore surface (Visez
69 et al., 2020). The agglomeration process may increase the allergenic potential of airborne spores and
70 pollen due to chemical reactions, increasing the health risk for allergy sufferers (Sénéchal et al.,
71 2015).

72

73 The arid regions of Northern Africa are some of the largest sources of desert dust in the world. These
74 regions emit about 800 Tg yr^{-1} , corresponding to approximately 70% of the annual, global dust
75 loading (Prospero et al., 2014; Ryder et al., 2019). A large fraction (~ 182 million tons yr^{-1}) of these
76 emissions moves westward, ~ 2500 km across the Atlantic Ocean, extending in a continuous AD
77 plume over the Caribbean basin (Yu et al., 2015). Similarly, the transport of AD over Europe has a
78 clear seasonality whereby such events are more frequent from late autumn to early winter (February
79 to June) (Escudero et al., 2005). With climate change contributing to further desertification, not only
80 on the Africa continent, but in Asia and other parts of the world, dust incursion events will likely
81 increase in intensity and duration in the coming decades.

82

83 The majority of studies that have evaluated the transport of bioaerosols by AD have used samplers
84 that captured the particles on substrates that were subsequently analyzed in the laboratory under a
85 microscope or using Deoxyribonucleic acid (DNA) analysis. These analysis methodologies are the
86 most robust for identifying specific taxa of biological spores; however, online techniques offer the
87 advantage of larger sample sets that can be evaluated in much higher temporal resolution. Techniques
88 that use Ultra-violet Laser Induced Fluorescence (UV-LIF), such as the Wideband Integrated
89 Bioaerosol Spectrometer (WIBS), provide detailed information on the size, shape and fluorescence
90 intensity of individual particles in real time (Kaye et al., 2004). The recent investigation by Morrison
91 et al. (2020) employed a WIBS that was situated at the Sao Vicente Cape Verde Atmospheric
92 Observatory, off the west coast of central Africa, measuring continuously from September 2015 to
93 August 2016. Their measurements found strong seasonal changes in absolute concentrations of
94 fluorescing aerosol particles (FAP) with significant enhancements during winter due to the strong



95 island inflow of air masses originating from the African continent. Their results indicate that the
96 relative contribution of bioaerosol material in dust transported across the tropical Atlantic throughout
97 the year is relatively uniform, consisting mainly of mixtures of dust and bacteria and/or bacterial
98 fragments. They support their conclusions by comparing the WBS measurements with those from a
99 Laser Ablation Aerosol Particle Time of Flight mass spectrometer (LAAP-ToF). The latter
100 measurements show a high correlation between particles with mixed bio-silicate mass spectral
101 signatures and UV-LIF bio-fluorescent signatures, leading to the conclusion that the FAP
102 concentrations are dominated by these mixtures.

104 The measurements reported here, in our current study, complement those of Morrison et al. (2020)
105 with results from locations farther down-wind than their study site of Cape Verde. Our objectives are
106 to *1) expand the database of real time measurements related to long-range transported African
107 dust and the FAP associated with these events, 2) evaluate the relative changes in the multi-faceted
108 patterns of fluorescing particles, measured with the UV-LIF technique, as they relate to the air
109 mass sources and ages, 3) introduce new metrics, unique to the UV-LIF technique that provide
110 additional quantification of the FAP properties and 4) compare the real time fluorescence
111 signatures to those bioaerosols measured with off-line techniques.*

113 **2.0 Measurement locations, sensor description and analysis methodology**

114 **2.1 Study zones**

115
116 The Caribbean measurement site is the Cape San Juan (CSJ) atmospheric observatory (18°22.85'N,
117 65°37.07'W and 60 m, asl) located on the most northeastern point on the coast of Puerto Rico (PR).
118 The European measurements were made at the University of León, León, Spain, located in the
119 northwest region of the Iberian Peninsula (42° 36' N, 05° 35'W and 838 m, asl). Cape San Juan is a
120 remote, coastal research site managed by the Atmospheric Chemistry and Aerosols Research (ACAR)
121 group at the University of Puerto Rico – Rio Piedras Campus (UPR-RP). This measurement site has
122 been frequently used for sampling aerosols of non-anthropogenic origin (Novakov et al., 1997;
123 Mayol-Bracero et al., 2001; Allan et al., 2008) because the predominate airflow is from the northeast
124 and the particles are typically those generated from the ocean. i.e. sea salt, non-sea salt sulfates and
125 organic carbon (Allan et al., 2008) Furthermore, CSJ is also a recognized site for the World
126 Meteorological Organization's Global Atmospheric watch (WMO GAW) (Andrew et al., 2019) and
127 the National Aeronautics and Space Administration (NASA) network for AERONET, PANDORA,
128 and MPLNET.

129
130 The city of León is located in the northwest of the Iberian Peninsula. The climate has Mediterranean
131 maritime as well as continental features (Calvo et al., 2018). The sampling site is on the roof of the
132 Faculty of Veterinary, 15 m above ground level, at the León University Campus. The university is
133 located in the northeast suburban region of the city, which is largely devoid of local industrial
134 emissions, although there are daily anthropogenic emissions from vehicular traffic whose organic
135 compounds, like polyaromatic hydrocarbons (PAH), will fluoresce and need to be removed from the
136 evaluation as non-bioaerosols, as discussed below.

138 **2.2 Data sets and sources**

139
140 The data used in the present study comes from several sources of in-situ and remote sensor
141 measurements, as well as air mass back trajectories derived from archived meteorological data. Table
142 I lists the data sets that have been evaluated, their sources and the parameters that were extracted. The
143 primary source of particle information comes from the Wideband Integrated Bioaerosol Spectrometer
144 (WBS) since the main focus of our study is on the FAP that is being transported by AD. Ancillary
145 information about the origins of the air masses, complementary measurements of the particle optical



146 properties and the state of the local environments, e.g., meteorology, are included in order to better
 147 understand the impact of the AD intrusions.

148

149 Given the importance of the WIBS measurements, the following section focuses on the WIBS's
 150 measurement principles, limitations and uncertainties, the filtering necessary to minimize artifacts in
 151 the data, the corrections applied for dead-time losses and the parameters that are derived that provide
 152 tracking of the unique patterns that are found in the particle properties.

153

Table I
 Data sets used in the Analysis

155

156

Data Set Description	Data Source	Extracted Parameters	Measurement Sites
Single particle aerosol properties	WIBS-V ¹	Aerosol particle equivalent optical diameter, 0.5 – 30 µm, autofluorescence, Asphericity factor, non-FAP and FAP number concentrations.	PR and LUC
Fog properties	FM-120 ¹	Fog droplet equivalent optical diameter, droplet number concentration, liquid water content.	LUC
Aerosol Particle mass	MET-1 ² ,	Mass concentration in particles with aerodynamic diameter < 10 µm (50% cut size)	LUC
Filter samples	Hirst spore trap (VPPS 2000, Burkard) ³	Morphological identification of fungal spore and pollen taxa.	PR and León
Aerosol optical properties	Aethalometer ⁴ , AERONET Sun photometer ⁵	370 nm and 880 nm extinction coefficient, Multi-wavelength optical depth	PR
Local environments state parameters and radiation	Meteorological weather stations ⁶	Temperature, humidity, pressure, wind speed and direction and visibility	PR, LUC
MERRA-2	Modern-Era Retrospective analysis for Research and Applications version 2 ⁷	Column mass density of aerosol components (black carbon, dust, sea salt, sulfate, and organic carbon), surface mass concentration of aerosol components, and total extinction (and scattering) aerosol optical thickness (AOT) at 550 nm	PR, LUC
Air mass back trajectories	Hysplit ⁸	Location and meteorology at hourly intervals	PR, LUC

157

¹ Manufactured by Droplet Measurement Technologies, LLC, Longmont, CO

² Manufactured by Met One instruments, Grants Pass, OR

³ Manufactured by Lanzoni, Bologna, Italy and Burkard Scientific Ltd, Uxbridge, UK

⁴ Manufactured by McGee Scientific Inc, Berkely, CA

⁵ Manufactured by CIMEL Electronique, Paris, France

⁶ Manufactured by Vaisala Instruments and Davis Instruments, Hayward, CA, USA

⁷ https://disc.gsfc.nasa.gov/datasets/M2T1NXAER_5.12.4/summary

⁸ <https://www.ready.noaa.gov/index.php>



158 **2.3 Wideband Integrated Bioaerosol Spectrometer (WIBS)**

159

160 **2.3.1 Principles of operation, uncertainties and limitations**

161

162 The WIBS measurement principles are based on Ultraviolet light-induced fluorescence (UV-LIF)
163 (Kaye et al., 2005; Stanley et al., 2011). The current model, the WIBS-V differs from earlier models
164 only in how the data are formatted and how downtime losses are taken into account. The
165 supplementary material describes the WIBS in greater detail, along with the specific algorithms used
166 to filter and correct the measurements prior to analysis and interpretation. All WIBS models bring
167 individual particles into the instrument with an internal pump and direct them through a collimated
168 laser beam using aerodynamic focusing. The light scattered from each particle is used as a signal to
169 trigger two xenon flash lamps, which activate sequentially, illuminating the particle as it leaves the
170 laser beam with light filtered at 280 nm and 370 nm, respectively. Two detectors, one with a bandpass
171 filter at 310–400 nm and the other with a 420–650 nm filter, receive light emitted by autofluorescence
172 if there is material in the particle that is excited to fluoresce at one or both excitation wavelengths.
173 The equivalent optical diameter (EOD) is derived from the light scattered by the particle as it transits
174 the laser beam and an “asphericity/asymmetry factor” (AF) is derived from a quadrant detector that
175 is illuminated by the forward scattered light from this same particle.

176

177 A number of naming conventions have been introduced in the literature over the years for labeling
178 the fluorescence combinations that are possible with the WIBS measurements; however, they all
179 agree on using FL1 (Channel A) and FL2 (Channel B) to denote signals from the excitation at 280
180 nm, emissions at 310–400 nm and 420–650 nm, respectively, and FL3 (Channel C) to indicate signals
181 from excitation at 370 nm and emissions at 420–650 nm. As is often the case, the fluorescence from
182 a single particle may be a combination of any two or three of these excitation/emission pairs, leading
183 to as many as seven possible fluorescent types. Following the convention first proposed by Perring et
184 al. (2015), we will label the seven fluorescence types as A, B, C, AB, AC, BC and ABC throughout
185 the remainder of this presentation.

186

187 The two major sources of uncertainty are fluorescence artifacts and missed fluorescence signals due
188 to downtime. Both of these uncertainties, and steps taken to minimize or to correct for them, are
189 discussed in greater detail in the supplemental material, as well as in previous publications (Calvo et
190 al., 2018; Sarangi et al., 2022). In short, there are two types of fluorescence artifacts: 1) light detected
191 by the fluorescence detectors that wasn’t fluorescence from ambient particles and 2) light detected by
192 the fluorescence detectors that is produced by non-biological materials.

193

194 If the chamber where particles are illuminated by the flash lamps is not cleaned after regular use,
195 material may accumulate that will fluoresce, albeit at a fairly low level. Nevertheless, this
196 fluorescence represents a source of background noise that needs to be quantified and removed from
197 the signal produced by legitimate FAP. A second source of fluorescence artifacts is the light from the
198 Xenon lamps themselves, a small fraction of which can leak through the filters in front of the
199 fluorescence detectors since these filters are not 100% efficient at removing light at wavelengths
200 outside their wave band. Non-biological materials, such as polycyclic aromatic hydrocarbons (PAH)
201 or black carbon, which can also fluoresce when illuminated, are considered here as artifacts with
202 respect to differentiating them from fluorescing bioaerosols (Gabey et al., 2013; Perring et al., 2015;
203 Pöhlker et al., 2012; Toprak and Schnaiter, 2013). These artifacts cannot be completely removed from
204 the analysis but can be minimized by removing from the processing any particles whose fluorescence
205 falls below a preset threshold. As described in the supplementary material, we follow the
206 methodology of Perring et al., (2015) and Morrison et al (2020) by creating daily frequency
207 histograms of the FL1, FL2 and FL3 type FAPs and use a threshold that is the mode of the frequency
208 distribution plus nine standard deviations (9σ) as the minimum threshold that has to be exceeded
209 before a fluorescing event is accepted as valid.



210

211 The aforementioned uncertainty due to electronic deadtime is associated with the eight milliseconds
212 that is required to recharge after each Xenon lamp flash. During this period, if the lamps receive a
213 trigger signal, they will not discharge so if the particle passing through the chamber is an FAP, it will
214 not be identified as such since it won't be excited by the lamps. The WIBS registers the particle's
215 size but a statistical correction is needed to account for the fraction of particles each second that might
216 have been FAP but passed through the Xenon chamber during a "dead time". The supplementary
217 material discusses how this correction is derived.

218

219

220 2.3.2 FAP features extracted from laboratory bioaerosol studies

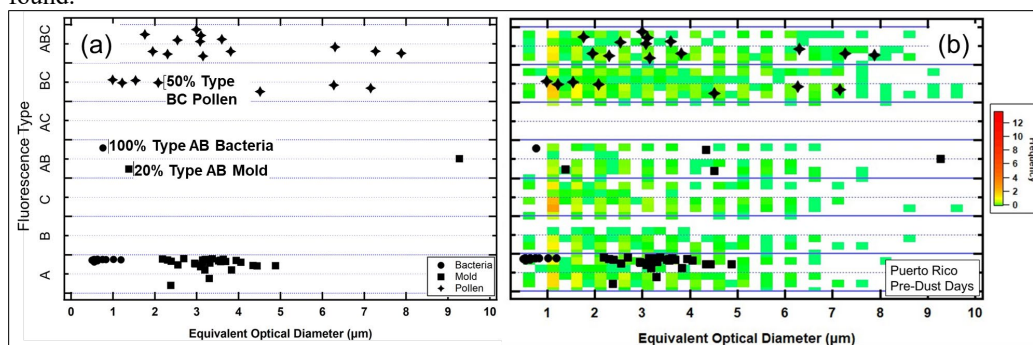
221

222 The FAP that were measured for the current study are assumed to be bioaerosols since we have taken
223 care to minimize artifacts; however, we are unable to *a priori* use the FAP properties to label the
224 particle as a specific type of bioaerosol, i.e. bacteria, fungal spores or pollen (BSP), to name the three
225 bioaerosol types most commonly found in the ambient environment (henceforth, we will group these
226 three types of bioaerosols and refer to them as BSP). We will take, instead, the same approach as in
227 Calvo et al. (2018) and refer to a specific FAP, for example, as "bacteria-like" or "fungi-like" when
228 a specific set of FAP metrics in the environmental measurements match the same metrics derived
229 from laboratory measurements.

230

231 We have reprocessed the data set that was used in the Hernandez et al. (2016) laboratory studies: 15
232 types of bacteria, 29 types of common fungal spores and 13 varieties of pollen, those typically found
233 in the natural environment. Figure 1a shows a composite of the fluorescence type and EOD of the 57
234 different varieties of BSP. Figure 1b shows an example of these same varieties superimposed on a
235 composite of measured FAP for a non-dust day in PR. This illustrates how the environmental data
236 clusters by FAP type and EOD in patterns very similar to those formed from the laboratory
237 measurements. The color scale in Fig. 1b denotes how frequently during the two-day period the FAP
238 types and EODs fell within the different FAP Type vs EOD regions. In this example, although the
239 environmental FAPs fall in regions where the lab data show bacteria, fungal spores and pollen, quite
240 a few of the FAP were in the regions of FAP types C and AB where very few of the lab results were
241 found.

242



243 **Figure 1. a) A BSP map showing how 15 bacteria, 29 mold and 13 pollen, of different taxa were measured in the**
244 **laboratory by a WIBS, as a function of FAP type and EOD and b) the same BSP map with FAP measurements from**
245 **a non-dust day in Puerto Rico plotted using the same definitions for FAP type and EOD. The color scale denotes how**
246 **frequently during the two-day period the FAP types and EODs fell within the different regions. In this example,**
247 **although the environmental FAPs fall in regions where the lab data show bacteria, mold and pollen, quite a few of the**
248 **FAP were in the region of FAP types C and AB where very few of the lab results were found.**

249

250 Although this method of comparing lab BSP patterns with environmental FAP cannot be construed
251 as a quantitative way to relate the WIBS measurements directly to BSP taxa, the laboratory data



252 provides a reference data set to which we can compare the measured BSP maps and evaluate relative
253 changes in patterns related to the AD intrusions.

254

255 **2.3.3 Working Hypothesis and Analysis Metrics**

256

257 From our work, and from those of others, we have sufficient measurements to conclude that
258 fluorescence intensity, regardless of the BSP taxa, is too variable to be used as a FAP property that
259 can be unequivocally or unambiguously related to a bioaerosol type. Likewise, the asymmetry factor
260 can be used as a rough indicator of asphericity but cannot provide finer structural details. The
261 fluorescence emission intensity is a complex interaction between the uniformity of the excitation
262 radiation over the surface of the FAP, the orientation of the particle as it is exposed to the incident
263 light, the non-isotropic nature of the fluorescence emissions and fluorescence quenching by material
264 mixed with the FAP (Lakowicz, 2006). Adding to these uncertainties are the observations from
265 microscopic analysis that a significant fraction of bioaerosols in the natural environment are not
266 intact, i.e. they are fractured pieces that can still fluoresce but with less intensity and shapes
267 unrepresentative of a whole particle.

268

269 The specific pairs of excitation/emission wavelengths employed in the WIBS were originally selected
270 by Kaye et al., (2005) due to their responsiveness to tryptophan (280 nm/310-400 nm) and
271 nicotinamide adenine dinucleotide (NAD; 370 nm/420-650 nm). Given that these two fluorophores
272 are omnipresent in plant tissues and microbiological cells they are good fluorescent markers for
273 bioaerosols. Nevertheless, the aforementioned uncertainties prevent more definitive speciation of the
274 FAP without complementary analysis using samples captured on filters or substrates that can undergo
275 microscopic analysis and classification by human observers or more intensive DNA analysis.

276

277 The advantage and power of the WIBS is the high-resolution information that it extracts from
278 individual particles, information that provides a statistically large sample that describes the sizes,
279 shapes and fluorescence patterns of an ensemble of particles in air masses whose properties can
280 change over relatively short time periods. Hence, even though there are large variations in these
281 properties, particle by particle, over periods as short as five to ten minutes, tens of thousands of
282 particles in the size range of 0.5 to 30 μm can be analyzed. Not only are the average properties
283 important, but their variances also contain valuable information about the composition and potential
284 source of these particles.

285

286 The analysis methodology that is selected to evaluate the WIBS data needs to be tailored to the
287 specific questions that are being addressed. Much progress has been made in the past 10 years in the
288 use of cluster analysis to identify features of the FAP, which are indirectly related to the type of
289 bioaerosol (Robinson et al., 2013; Crawford et al., 2015; Morrison et al., 2020). In our study, however,
290 we are asking a different set of questions, where knowing the type of bioaerosol is not as important
291 as understanding how the FAPs are transported and their properties transformed while in AD plumes.
292 Hence, we take a more heuristic approach whereby we concentrate on evaluating the nine parameters
293 (size, shape and seven FAP types) that can be extracted from individual particles, and we use these
294 to address the following questions:

295

- 296 1. Are the FAP that are found within the AD plumes, which inundate the Caribbean and Iberian
297 Peninsula, internally or externally mixed with the dust particles?
- 298 2. What features of the FAP change from normal background conditions to periods when the
299 AD is present?
- 300 3. Can the observed changes in the FAP properties be physically linked to the air mass histories?

301

302 Starting with the assumption that the properties of aerosols in dust plumes will differ significantly
303 from those of aerosols in the local environments of PR and León, *we hypothesize that 1) the*

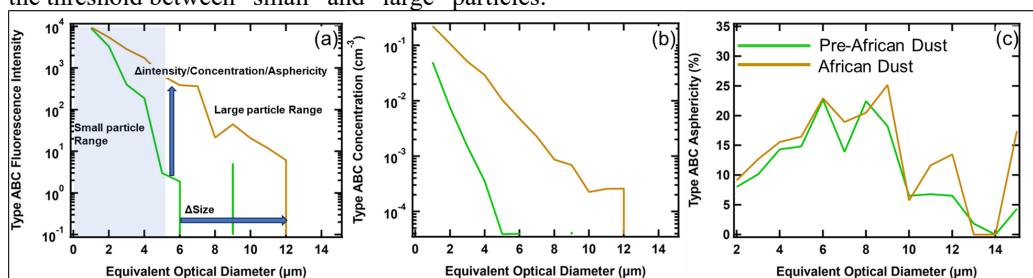


304 *bioaerosols that are in the dust plumes will be a mixture of bioaerosol types that differ from those*
305 *found in the PR or León ambient environments and 2) the majority of FAP in the AD plumes will*
306 *be attached or mixed with dust particles.*

307

308 To provide answers to these questions, and to test our working hypotheses, we focus on how the size
309 distributions of number concentration, fluorescence intensity and shape factor differ within the
310 populations of non-FAPs and FAP. These differences, between the PR and León sites, before and
311 during AD events, can be quantified using comparisons of the size distribution metrics. These metrics
312 can be visualized by referring to Fig. 2 that shows example size distributions of the FAP Type ABC
313 fluorescence intensity (Fig. 2a), number concentration (Fig. 2b) and shape factor (Fig. 2c), before
314 (green curve), and during (brown) a dust intrusion. An EOD of 5 μm has been arbitrarily selected as
315 the threshold between “small” and “large” particles.

316



317

318 *Figure 2. Examples of size distributions of Type ABC fluorescing aerosol particles before (green curve) and during*
319 *(brown curve) a dust intrusion, highlighting the features that are used as metrics in the analysis methodology. (a)*
320 *Average fluorescence intensity as a function of EOD. The vertical and horizontal blue arrows highlight increases in*
321 *intensity and size, respectively, with the incursion of AD. The size distributions have been divided into “small particle”*
322 *(shaded) and “large particle”.* (b) *average number concentration as a function of size and (c) Average asphericity as*
323 *a function of size*

324

325 The metrics that are derived from these size distributions and that we will use in our comparative
326 analysis are:

327

- 328 1. The change in fluorescence intensity, number concentration and shape factor of small
329 particles
- 330 2. The change in fluorescence intensity, number concentration and shape factor of large
331 particles
- 332 3. The change in the ratio between the concentration of small to concentration of large particles
- 333 4. The change in median diameter

334

335 From the examples shown in Fig. 2, for the FAP Type ABC, there is a significant increase in the
336 average fluorescence intensity and number concentration of small and large EOD particles with the
337 intrusion of AD; however, the shape factor size distributions are similar. As will be highlighted below,
338 these differences can be interpreted in the context of the relative mixture of FAP types and also how
339 these FAP are physically mixed with non-FAP.

340

341 2.4 Complementary measurements

342

343 Meteorological data, including temperature ($^{\circ}\text{C}$), relative humidity (RH, %), rain (mm), pressure
344 (mb), wind speed (WS, m s^{-1}) and wind direction ($^{\circ}$) were accessed from the weather station (Vaisala,
345 WXT 530) mounted on the top (30' from the ground) railing of an aluminum tower at the Puerto Rico
346 measurement site (CSJ).



347 The optical properties of the particles in PR were measured in situ with an aethalometer (Magee
348 Scientific) and remotely with a sun photometer. The aethalometer derived the absorption coefficients
349 from measurements of attenuations at 370 nm and 880 nm. The spectral Aerosol Optical Depth
350 (AOD), Ångström exponent, and volume size distributions were accessed from the sun/sky CIMEL
351 CE_318 Sun photometer that measures the direct solar irradiances with a field of view of
352 approximately 1.2° and the sky radiances at spectral wavelengths of 340, 380, 440, 500, 675, 870,
353 1020, 1640 nm, respectively. The CIMEL Sun photometer at CSJ is a component of NASA Aerosol
354 Robotic NETwork (AERONET) that provides long-term records of columnar aerosol optical
355 characteristics (Holben et al., 1998) since 2004.

356 In addition to the particle mass (PM) measurements made with the PM Beta monitor at the Junta de
357 Castilla and León air quality stations, an FM-120 fog monitor was operated in parallel with the WIBS
358 in León. The FM-120, developed by Droplet Measurement Technologies LLC, measures the EOD of
359 individual environmental particles from 2 - 50 µm. The FM-120 was originally developed to measure
360 fog droplet properties; however, the measurements are not specific to fog and in the presence of dust
361 particles will measure their size distributions but with a larger uncertainty because these particles will
362 not be spherical.

364 Fungal spores and pollen were collected with Hirst samplers (Hirst, 1952) in PR and Leon where they
365 were subsequently analyzed and classified by inspection under a microscope.

367 **3.0 Results**

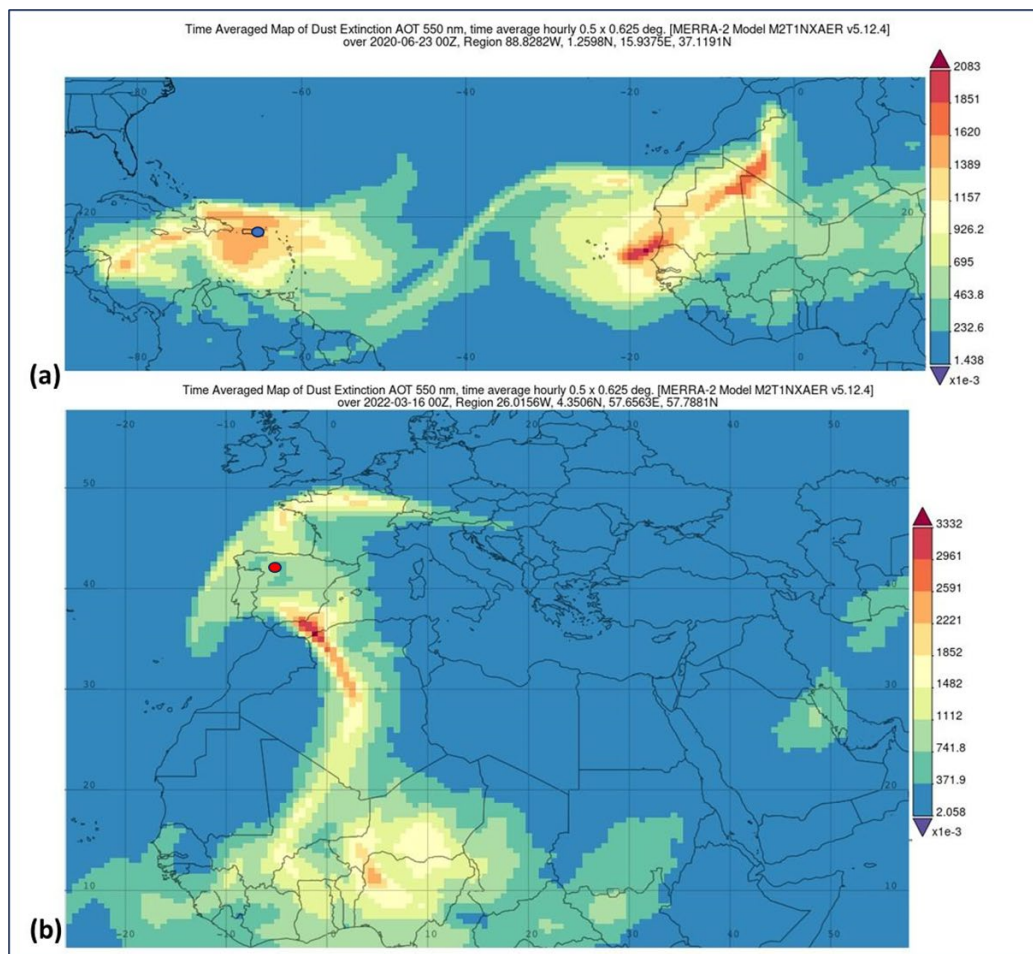
369 Prior to delving into the details of the in situ WIBS measurements, we use remote sensing data to
370 provide the complementary evidence for the large dust incursions on those days where the WIBS
371 measured particle properties that were anomalous when compared to those normally encountered
372 during the respective summer and spring seasons in PR and León.

374 **3.1 Remote Sensing Observations**

376 Satellite images from the Suomi National Polar-Orbiting Partnership (Suomi NPP,
377 <https://ncc.nesdis.noaa.gov/VIIRS/>) show a high frequency of dust intrusions over the North Atlantic
378 during the spring and summer of 2020. One of these events was an intense, widespread dust plume
379 that was observed over the eastern North Atlantic, clearly originating from the African Sahara region.
380 The June 23 2020 satellite image, shown in Fig. S1, reveals a large region of dust over the Caribbean
381 with another extensive layer of dust leaving northern Africa. This dust plume, which at some point
382 had a size equivalent to the area of continental USA (around 8,000,000 km²), impacted the Caribbean
383 region and parts of South America, Central America, Gulf of Mexico, and the Southern USA from
384 June 21 to July 1. On June 20, when the first dust pulse began to affect the Caribbean, a second dust
385 layer was clearly seen leaving Africa (Fig. S1a), but smaller in extent than the first one (Yu et al.,
386 2021). This second dust layer impacted the same area as the first plume from 26th of June to July 1.
387 On June 22-23, PR received the leading edge of the dust plume followed by a second dust inundation
388 on June 28-29 (Fig. S1a). This event has been reported by a number of research groups (Francis et
389 al., 2020; Pu and Jin, 2021; Yu et al., 2021; Asutosh et al., 2022). According to Pu and Jin (2021), the
390 meteorology behind this dust plume is unprecedented: the surface wind speed (the strongest since the
391 previous 42 years) increased the dust emissions in Africa followed by an intensified African Easterly
392 Jet (AEZ) moving the dust plume westward. Francis et al (2020) posit that the extreme dust event
393 was caused by the development of a subtropical high-pressure system over northwest Africa that led
394 to the strong north-easterlies that were sustained over the Sahara generating four days of continuous
395 dust emissions. This dust event is also clearly seen from the Modern-Era Retrospective analysis for
396 Research and Applications, Version 2 (MERRA-2), shown in Fig. 3a for June 23, 2020, which shows
397 clearly the same patterns that were derived from the Suomi NPP satellite products (Fig. S1a).



398



399 **Figure 3** The Aerosol Optical Thickness (AOT) at 500 nm, derived from the MERRA, show the air masses carrying
400 dust from the African continent over (a) Puerto Rico, on 23 June, 2020 and then (b) another plume traveling over the
401 Iberian Peninsula and Southern Europe on 16 March 2022. The blue and red markers indicate the locations of the
402 PR and Leon measurement sites, respectively.
403

404 The Iberian Peninsula is also frequently inundated by Saharan dust outbreaks due to its proximity to
405 large dust-emitting areas of the Sahara and Sahel deserts and to the atmospheric dynamics and
406 meteorological conditions (Alastuey et al., 2016; Escudero et al., 2007; Querol et al., 2014; Rodríguez
407 et al., 2001). Previous studies reported that most of the outbreaks occur between spring and summer
408 when the dust transportation is regulated by the anticyclonic activities over the east or southeast of
409 the Iberian Peninsula (Lyamani et al., 2015; Rodríguez et al., 2001; Salvador et al., 2013). In winter,
410 Saharan dust intrusions are scarce and are usually dominated by the cyclonic activities over the west
411 or south of Portugal (Díaz et al., 2017; Rodríguez et al., 2001). However, in late winter, 2022, an
412 unprecedented dust storm impacted the Iberian Peninsula. The dust layer traveled over a large portion
413 of Europe, initially on 16-17 March 2022, followed by a secondary dust plume that covered an
414 extended region 27-30 March 2022. The satellite imagery obtained with the Suomi NPP clearly shows
415 the dust layer over the Iberian Peninsula on March 16 and 17 2022 (Figs S1b and c) and also seen in
416 the images derived from the MERRA-2 data (Fig. 3b)
417
418

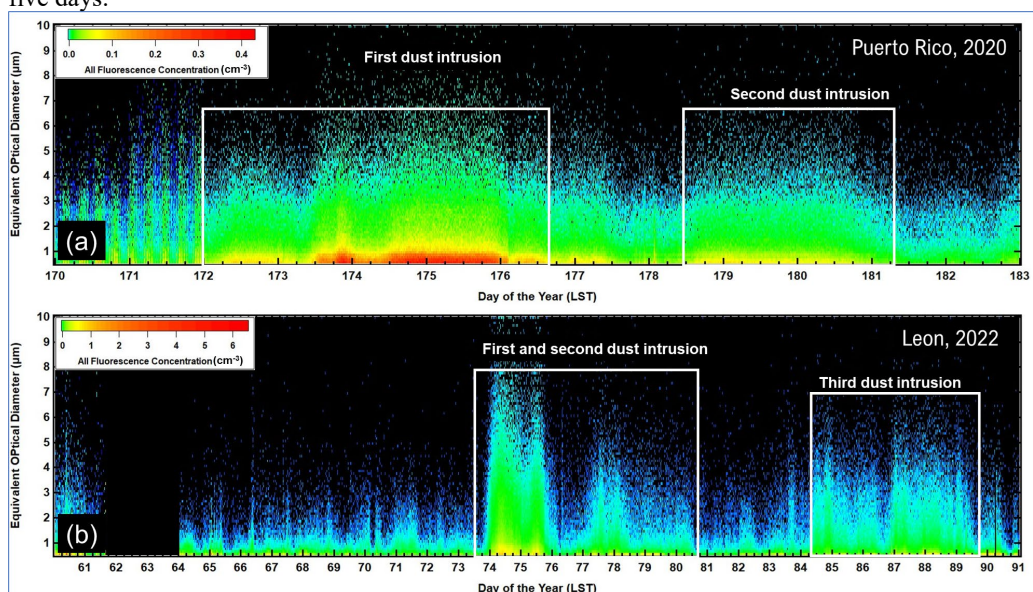


419 3.2 WIBS Observations

420

421 The arrival of the AD over PR and León is reflected in large increases in the number concentration
422 as seen in the time series of the FAP size distributions shown in Figs. 4a and b, respectively. In PR,
423 the first dust intrusion is seen on June 21 (day of the year, DOY, 172) and then approximately six and
424 a half days later the second AD layer arrives on June 27 (DOY 179). Likewise, in León the first AD
425 incursion is detected by the WIBS on March 16 (DOY 74) and lasts for more than five days. This
426 event was followed 10 days later by the second inundation on March 26 (DOY 84) lasting another
427 five days.

428



429 *Figure 4. a) Time series of the size distributions of FAP number concentrations measured at PR, Puerto Rico. The*
430 *white boxes delineate the periods when the satellite and back trajectory analyses indicate that AD has arrived over the*
431 *island, b) similar to (a) but for FAP concentrations measured in León, Spain.*

432

433 The influence of these dust incursions on the general aerosol population can be observed by the
434 changes in particle asphericity, shown in the size distributions of the shape factor (percent asphericity)
435 drawn in Fig. 5. These size distributions are of the non-FAP aerosols and show that the shape factor
436 increases from quasi-spherical, i.e. shape factor < 10%, to > 30% during the periods of AD in PR and
437 León.

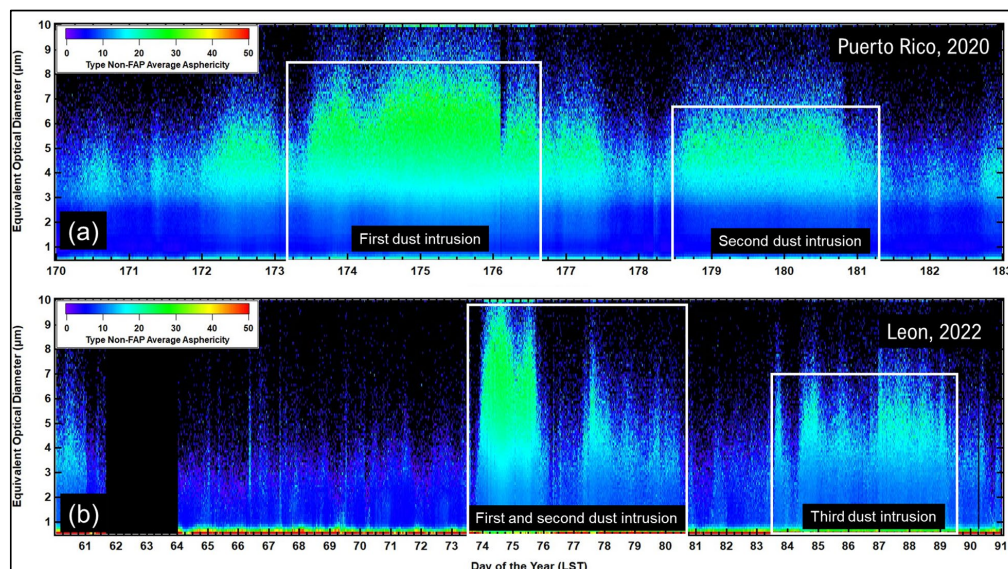
438

439 The size distributions shown in Fig. 6 highlight the similarities and differences between the PR and
440 León aerosol populations and illustrate how the arrival of the AD significantly changes how the non-
441 FAP and FAP number concentrations vary with size. The PR and León distributions are drawn in
442 black and green, respectively, solid lines for pre-dust events, dashed for dust intrusions. The pre-dust
443 size distributions of non-FAP aerosol (Fig. 6a) are almost identical at both sites, with a small fraction
444 of the León particle population larger than those in PR. The arrival of dust leads to almost two orders
445 of magnitude increase in both the PR and León concentrations, over all sizes, and brings significant
446 numbers of particles larger than 10 µm. For the non-FAP aerosols the relationship between
447 concentration and size during the AD event is nearly the same for PR and León.

448

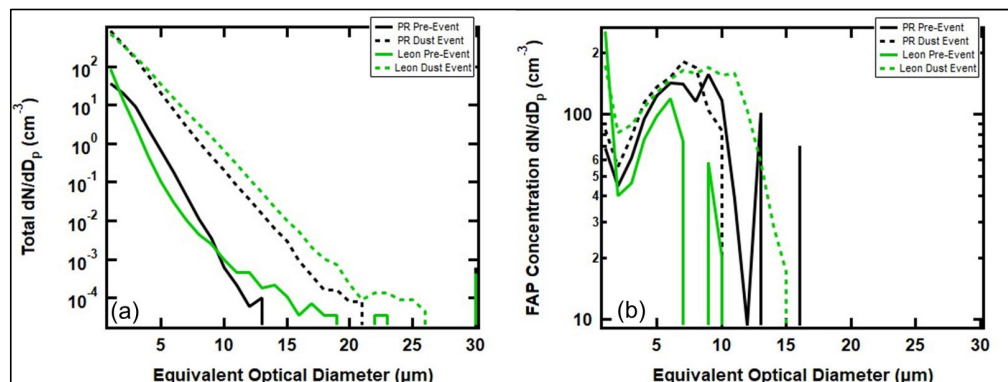


449



450 *Figure 5. a) Time series of the size distributions of non-FAP asphericity measured at PR, Puerto Rico. The white boxes*
 451 *delineate the periods when the satellite and back trajectory analyses indicate that AD has arrived over the island, b)*
 452 *similar to (a) but for non-FAP asphericity measured in León, Spain.*
 453
 454

455



456 *Figure 6. Average size distributions in PR and León, before and during AD events for the (a) number concentrations*
 457 *of the total aerosol population in the size range of the WIBS, b) number concentrations of only FAP.*
 458

459

460 A comparison of the FAP size distributions (Fig. 6b) tells a very different story. Below 2 μm, the
 461 León FAP concentrations exceed those in PR by about a factor of four; however, the PR FAP pre-
 462 dust size distribution is much broader than the FAP in León, extending beyond 10 μm while the FAP
 463 in León ends around 7 μm. The arrival of the dust does little to change the general shape of the PR
 464 size distribution other than slightly narrowing it. In contrast, the León size distribution broadens
 465 significantly out to 15 μm. This difference between PR and León offers the first clue that there is a
 466 difference between PR and León with respect to how FAP are mixed with non-FAP in the AD plumes
 467 that inundate these two sites.

468

469

470

471

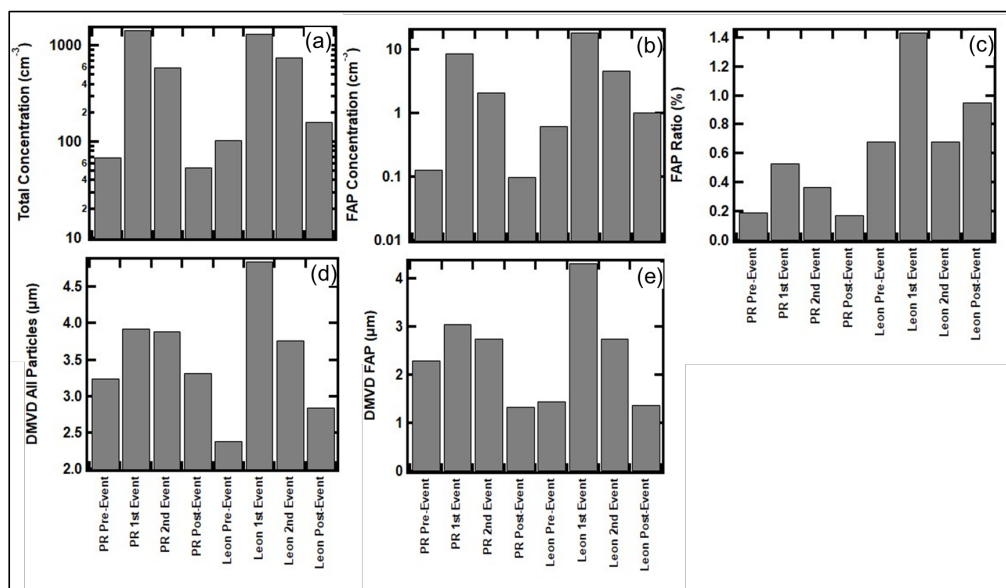
The average number concentration of non-FAP and FAP, the ratio of FAP to non-FAP concentrations,
 and the median, equivalent optical diameters (MEOD) of non-FAP and FAP are bulk parameters that
 are extracted from the size distributions and are shown in Fig. 7 for periods with no influence from
 AD and those in the presence of dust. Whereas Figs. 6a and b only showed one period with no-dust



472 and one period with AD for PR and León, Fig. 7 includes the second periods of dust, for the two
 473 locations, accompanied by periods before and after the dust intrusion. This more comprehensive data
 474 set demonstrates that for both PR and León there are clear differences in the bulk parameters under
 475 no-dust and dust conditions. The total and FAP number concentrations increase by an order of
 476 magnitude in PR and León when the AD arrives, as compared to the no-dust periods (Figs. 7a and b).
 477 The ratios of FAP to all particles (Fig. 7c) increase by a factor of two in PR and León under AD
 478 conditions; however, the León FAP ratios are three times larger than PR in the presence of AD.
 479 Likewise, although the arrival of dust in PR and León leads to increases in the average MEOD of all
 480 particles and FAP (Fig. 7c and d), the increase in León is much more than in PR, 200-300% vs 30%,
 481 respectively.

482

483

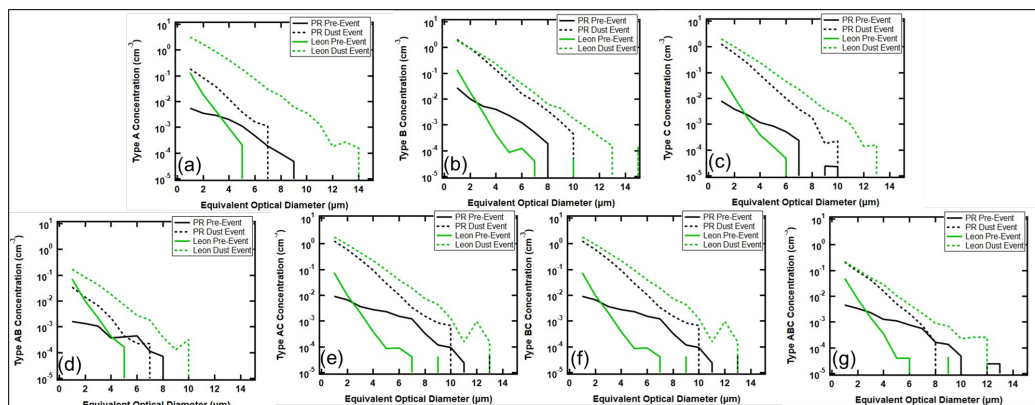


484 **Figure 7. Average values of derived parameters from WIBS measures before, during and after AD events. (a) Total**
 485 **number concentrations, (b) Number concentrations for all FAP, (c) Ratio of all FAP to all particles, (d) Median volume**
 486 **diameter (DMVD) of all particles between 0.5 and 30 μm and (e) DMVD of all FAP between 0.5 and 30 μm)**
 487

488 Figure 8 takes a closer look at the FAP, stratifying them by the fluorescing types. The pre-dust event
 489 aerosols in PR and León contain all seven types of FAP. Those measured in PR extend out to 10 μm,
 490 regardless of type. In León, at EODs < 2 μm, the number concentrations are always higher in
 491 concentration than those in PR but never exceed 7 μm in size. The arrival of the AD significantly
 492 changes the shapes of the size distributions, especially those in León, by bringing FAP that extend
 493 out to > 10 μm. The primary impact on the PR aerosols is to increase their number concentrations
 494 across all sizes and FAP types, while making little changes in the maximum EOD, except for the FAP
 495 Type B whose maximum EOD increases from 8 to 10 μm. The change in the size distributions of
 496 Type AC (Fig. 8e) with the arrival of the dust is particularly noticeable in PR and León. During non-
 497 AD periods the concentrations of Type AC FAPs is quite low at both measurement sites and then the
 498 arrival of AD increases the concentrations by several orders of magnitude, suggesting that the dust
 499 FAPs vary from the normal, background FAP in concentrations, size and types.

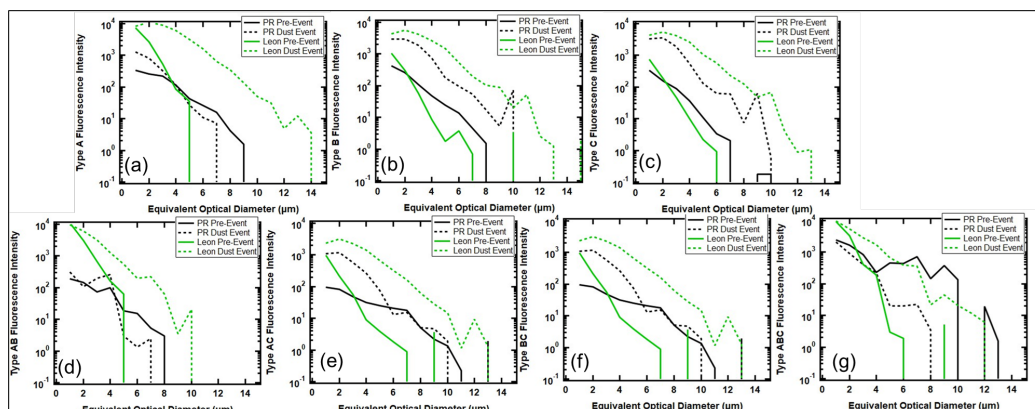


500



501 **Figure 8.** Average number concentration size distributions of FAP in PR (black) and León (green), before (solid) and
 502 during (dashed) AD events for (a) Type A, (b) Type B, (c) Type C, (d) Type AB, (e) Type AC, (f) Type BC, (g) Type
 503 ABC.
 504
 505

506



507 **Figure 9.** Average fluorescence intensity of size distributions in PR (black) and León (green), before (solid) and
 508 during (dashed) AD events for (a) Type A, (b) Type B, (c) Type C, (d) Type AB, (e) Type AC, (f) Type BC, (g) Type ABC.
 509

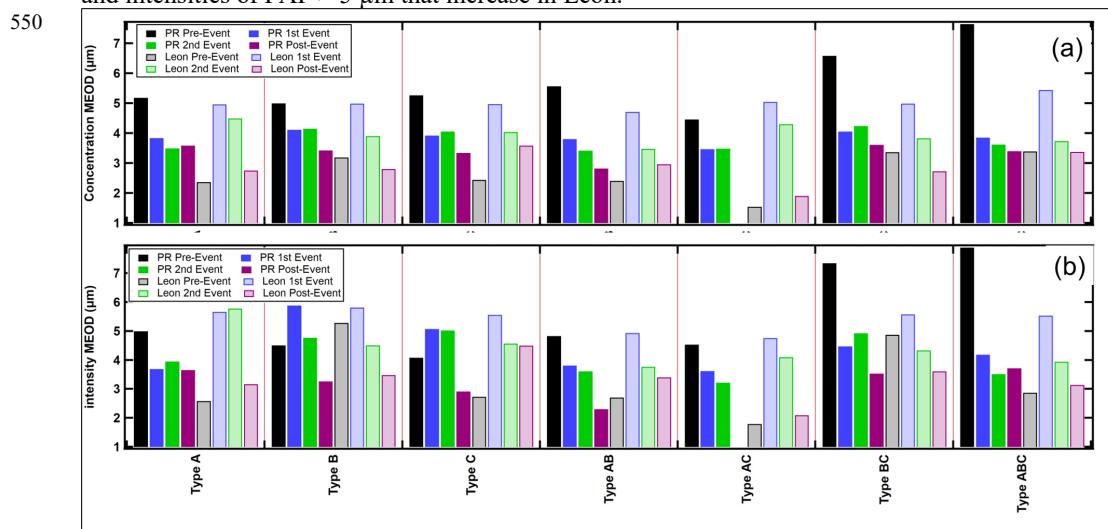
510 Similar to Fig. 8, Fig. 9 illustrates the average fluorescence intensity as a function of size for the seven
 511 FAP types. Keeping in mind that the average fluorescence intensity is unrelated to the average number
 512 concentration, we observe that the average fluorescence intensity of the León pre-dust aerosols are
 513 greater than those in PR in the size range less than 2 μm, i.e., the difference in fluorescence intensity
 514 below 2 μm is not a result of higher concentrations in León, but possibly a different type of FAP.
 515 Similar to the comparison of the number concentrations, the PR FAP extends out beyond 8 μm for
 516 all types. The size distributions of Types B and C aerosols measured in PR and León, pre-dust, are
 517 quite similar in shape whereas the León size distributions are quite different from those in PR for the
 518 other types, suggesting a dissimilar population of bioaerosol taxa at the two locations. The arrival of
 519 the dust leads to shifts in the size distributions that are similar for the PR and León Types B and C;
 520 however, the León fluorescence intensity increases by more than two orders of magnitudes while the
 521 PR intensities are about a factor of 10 higher in magnitude. Whereas the León intensities of all FAP
 522 types broaden from a maximum of 6 μm out to more than 10 μm, the PR distributions show little
 523 broadening except for Types B and C. The primary difference between the pre-dust and dust events
 524 in PR is an increase in intensity of FAP < 5 μm as compared to the increase in intensity over all sizes
 525 with the León distributions. The difference between the PR and León changes in size distributions
 526 with the arrival of the AD is particularly striking for the Type ABC aerosol. The León distributions
 527 broaden from a maximum of 6 μm to 12 μm, the PR distributions narrow from 10 μm to 8 μm and



528 the average fluorescence intensity decreases over this size range by more than a factor of 10. These
529 contrasts between the PR intensity size distributions with those of León provide an additional piece
530 to the puzzle associated with how FAP are mixed with AD when the plumes reach the respective
531 locations.

532
533 A comparison of the shape factor size distributions, shown in Fig. S4, informs us that FAP types A
534 and AB are quasi-spherical (fluorescence intensity < 15%) while the other FAP types are more
535 aspherical (>15%) at EODs between 6 μm and 10 μm . There is not a significant difference between
536 PR and León FAP, either pre-dust or during the AD events.

537
538 Figure 10 highlights the transitions in the size distribution shapes, for all FAP types, by comparing
539 the MEOD metric derived for all dust and no-dust periods, similar to what was shown in Figs. 7d and
540 e. In this case, however, the MEODs were extracted from the size distributions of FAP number
541 concentration (Fig. 10a) and fluorescence intensity (Fig. 10b). There is a stark difference seen
542 between the background MEODs of number concentration and fluorescence intensity when
543 comparing the background (no-dust) values from PR and León. The MEODs range between 5 μm
544 and 8 μm in PR while the León MEODs are much smaller, between 2 μm and 5 μm . The second
545 major difference between the PR and León MEODs is that the PR MEODs decrease with the intrusion
546 of dust, with all FAP types except B and C, while the MEODs increase over all the FAP types. These
547 differences were reflected in the size distributions where we see significant increases in the number
548 concentration and fluorescence intensity of the FAP < 5 μm in PR whereas it is the concentrations
549 and intensities of FAP > 5 μm that increase in León.



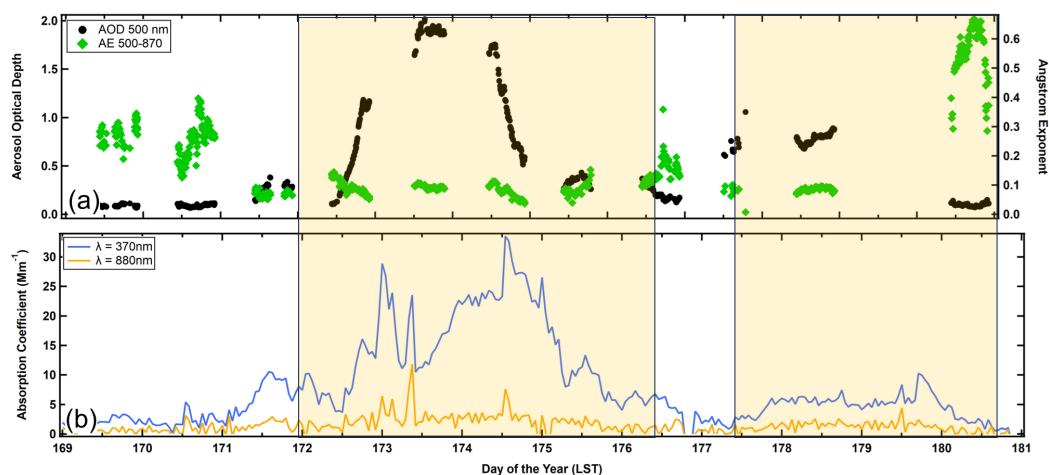
551 *Figure 10. (a) Average median equivalent optical diameters (MEOD) of the size distributions of the number*
552 *concentrations for the seven FAP types. The color coding delineates the locations (PR and León) and dust event*
553 *conditions (before, during and after). (b) Same as (a) except the MEODs are from the size distributions of the average*
554 *fluorescence intensity.*
555

556 3.3 Complementary Meteorological and Aerosol Observations

557
558 An evaluation of the meteorological state parameters and winds saw no indication of the dust arrival
559 in PR or León, i.e., we observe no significant difference in temperature, relative humidity, wind speed
560 or wind direction. Hence, the meteorological properties of the dust layer do not appear to have a
561 noticeable impact on the local meteorology in PR or León (Fig. S5 and S6).



562



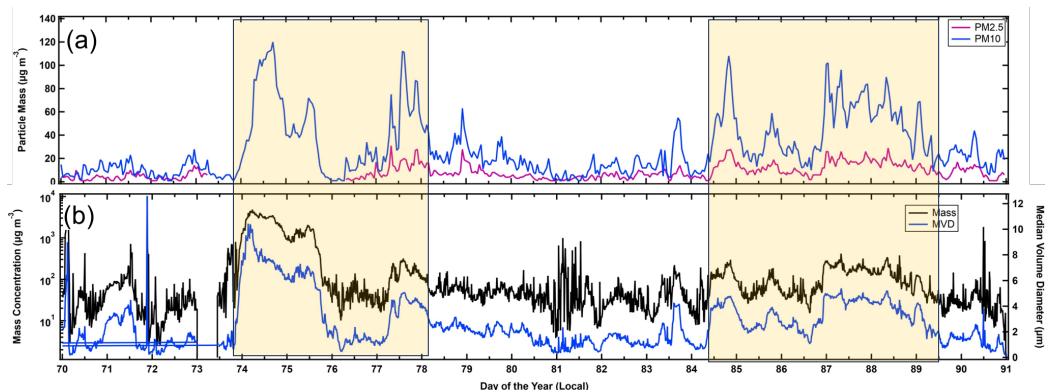
563 **Figure 11. Time series in Puerto Rico of (a) the aerosol optical depth (AOD) at 500 nm wavelength (black markers),**
564 **Ångström exponent derived from the 500 nm and 870 nm AODs (green markers) and (b) Absorption coefficients at**
565 **wavelengths of 370 nm (blue) and 880 nm (orange). The shaded areas demarcate the time periods when AD was in**
566 **the region.**

567

568 Figure 11 illustrates the impact of the AD on the aerosol optical properties in PR where the shaded
569 regions delineate the time periods with AD. In PR the trends in the extinction coefficients (Fig. 11b,
570 blue and orange curves) suggest that the leading edge of the AD layer might have already arrived at
571 the measurement site a day earlier than the measurements from the WIBS indicate (Figs. 4a and 5a).
572 The 370 nm extinction coefficient shows an increase on DOY171, reaching a peak in the middle of
573 the day before decreasing in the evening. The 880 nm extinction coefficient does not show the same
574 trend because dust absorbs at 370 nm and very little at 880 nm, although the light scattering at 880
575 nm produces a lower intensity extinction coefficient. There were no increases in wind speed or shifts
576 in wind direction (Fig. S1) that could indicate that these might be anthropogenic in origin, or possibly
577 local dust. This pattern is also reflected by a small increase in the aerosol optical depth (Fig. 11a,
578 AOD, black markers), which follows the same trend. The AOD, measured with a sun photometer,
579 can't distinguish the actual altitude where these new particles might be located; hence, these could be
580 dust particles that had been transported into the boundary layer where they would be measured by the
581 MET-1 OPC. The main body of the AD layer, identified from the WIBS measurements (Figs. 4a and
582 5a) arrived on DOY172, where it is also seen clearly in the 370 nm extinction measurements (Fig.
583 11b) and the AOD (Fig. 11a). Note that the AOD and 370 nm extinction coefficients, although
584 roughly correlated in time, will not follow the same trends if dust in the boundary layer and free
585 troposphere is arriving with a different periodicity than the dust that is sedimenting or being
586 transported downward by larger scale eddies. The other aerosol parameter plotted in Fig. 11a is the
587 Ångström exponent derived from the 500 nm and 870 nm AODs. This parameter is roughly inverse-
588 related to the average, median size of the aerosol particles. We observe in Fig. 11a (green markers),
589 that during periods with no-dust, the exponent is larger than during periods of dust, an expected result
590 given the significant increase in average EOD that was observed from the WIBS measurements.



591



592 **Figure 12.** Time series in León of (a) PM2.5 (magenta) and PM10 (blue) and (b) particle mass concentration (black
593 black curve) and median volume diameter (blue) measured with the FM120 in León. The shaded areas demarcate the time
594 periods when AD was in the region.
595

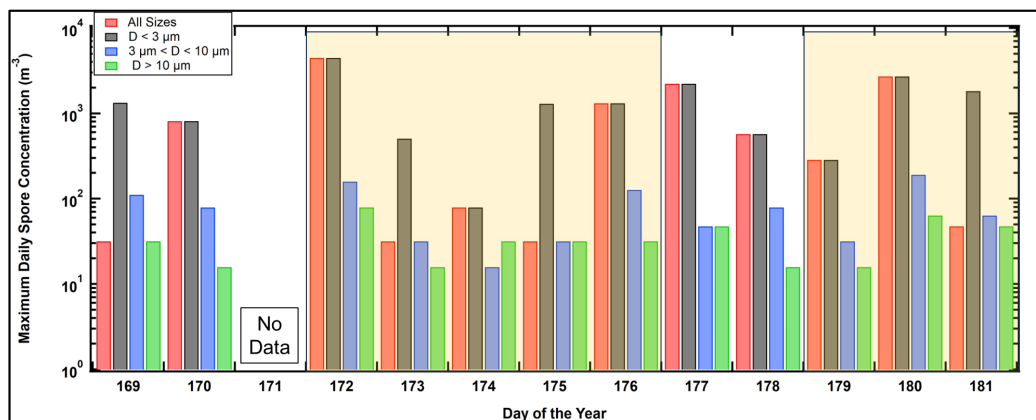
596 The AD incursion over León is reflected in the PM2.5 and PM10 measurements (magenta and blue
597 curves, respectively) shown in Fig. 12a. Unlike the trends in the PM measured in PR, there is a clear
598 periodicity in León where daily peaks are observed on most days, regardless if the AD is present;
599 however, during the AD, the maximum PM is four to ten times larger than when the AD isn't present.
600 Given that there doesn't appear to be any correlation with meteorological parameters, the trends are
601 likely the result of changes in the depth of the boundary layer. As this layer grows during the day,
602 due to radiative heating, the AD that is aloft in the free troposphere mixes downward and increases
603 the PM near the surface. Figure 12b shows the mass concentrations derived from the FM120 size
604 distributions (black curve) and the median volume diameter (blue curve). This complementary set of
605 measurements, independent of the WIBS or air quality PM measurements, is highly correlated with
606 the results from both instruments and show that the MEOD increases from $< 3 \mu\text{m}$ to $> 5 \mu\text{m}$ when
607 the AD arrives. The very large mass concentrations are a result of the particles $> 10 \mu\text{m}$, as can be
608 observed in the time series of the FM120 size distributions (Fig. S7). Between DOY 74 and 75 the
609 size distribution is clearly bimodal with one peak at $5 \mu\text{m}$ and the other between 20 and $30 \mu\text{m}$. These
610 large particles are what drive the very high PM values seen in Fig. 12b, which are much larger than
611 registered by the PM10 sensors in the air quality station.
612

613 3.3 Hirst Sampler Observations

614
615 The timeseries of micro and macroconidia fungal spore concentrations, collected in PR and sorted by
616 size range, are drawn in Fig. 13. The microconidia $< 3 \mu\text{m}$ (black bars) are always the highest in
617 concentration, followed by the microconidia $> 3 \mu\text{m}$ and microconidia $< 10 \mu\text{m}$ (blue) and the
618 macroconidia $> 10 \mu\text{m}$ (green). The shaded regions are highlighting the periods of AD. There are
619 differences in the concentrations of these fungal spores when comparing periods with and without
620 AD, but they are subtle. Given that the dust plume mixes with the ambient aerosols *a priori* we have
621 no reason to expect the spore concentrations to increase or decrease. More significant is the
622 appearance of spore types that were not identified during the no-dust periods. Table II provides more
623 explicit detail regarding the redistribution of spore types. More important than the total number
624 concentrations are the appearance of new spore types and disappearance of others during the AD
625 episodes. These are highlighted in the table, blue when periods of AD lack spores during no-dust
626 periods, and red when spore types appear that were not in the no-dust periods. In addition, cells in the
627 table are shaded orange when a spore type increases by $\geq 100\%$ from no-dust to dust.



628



629 *Figure 13 Time series of spore concentrations, stratified by size, in Puerto Rico. The shaded regions are periods of AD*
 630 *inundation.*

631

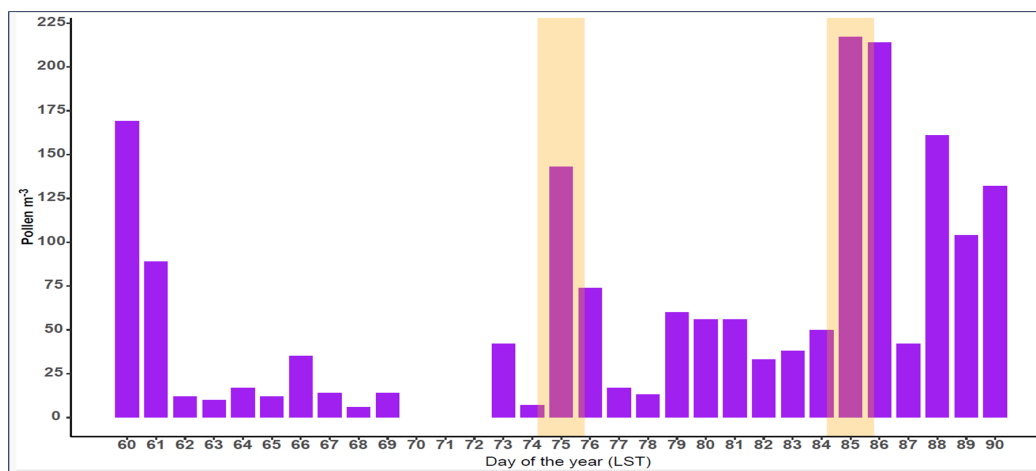
632 There are two spore types, *Dreschlera Helmitosporum* and *Fusarium* that were measured on the no-
 633 dust days but were no longer identified during AD. Likewise, with the arrival of the dust, five new
 634 spores appeared that were not previously seen in the background environment: *Erysiphe/Oidium*,
 635 *Periconia*, *Spegazzinia*, *Tetrapyrgos* and *Chaetomium*. Of these, the *Erysiphe/Oidium* had the highest
 636 concentration, four times higher than the others.

637

638 In León during March 2022 a total of 9 pollen types were identified. *Cupressaceae* and *Populus*, both
 639 in their main pollen season (MPS), were the most abundant types (abundance relative: 43% and 40%,
 640 respectively). The other pollen types presented relative abundance values lower than 5%. Some pollen
 641 types such as *Alnus*, *Corylus*, *Fraxinus* and *Ulmus* were finishing their MPS, whereas *Platanus*,
 642 *Poaceae* and *Pinus* were starting it. *Salix* was in the MPS during this period, although it is not an
 643 abundant pollen in the ambient atmosphere. During the two AD intrusions, an increase in pollen
 644 concentration compared to the previous day (DOY 75: >1000%; DOY 85: 300%) was registered
 645 (Figure 14). During the first one, most of the counted pollen belonged to *Cupressaceae*. Nevertheless,
 646 during the second AD inundation the predominant pollen was *Populus*. Days with AD inundation did
 647 not show differences in airborne pollen diversity compared to days without AD intrusion.

648

649



650 *Figure 14. Time series of daily average pollen concentrations in León during the selected period. The yellow shaded*
 651 *regions indicate the AD inundation.*

652



653

Table II

654

Number Concentration (m^{-3}) of Fungal Spores in Puerto Rico (Maximum daily values)

655

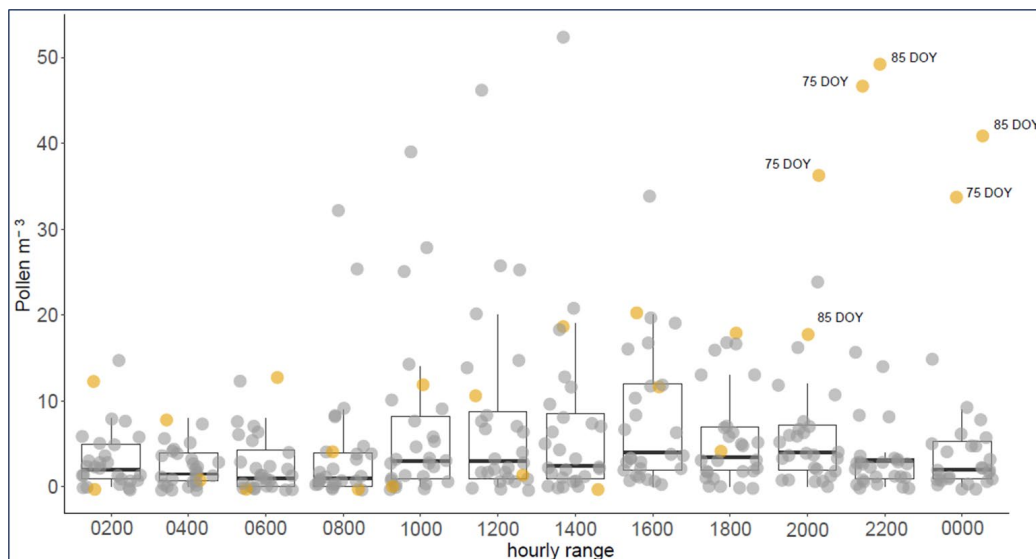
Macroconidia >10 μm	No AD	AD	Change %	Microconidia 3-10 μm	No AD	AD	Change %	Microconidia <3 μm	No AD	AD	Change %
Hifas fragmentos	64	48	-25	Curvularia	16	80	400	Ascosporas	3844	1621	-58
Cercospora	207	96	-54	Dreslera Helmitosporum	16	0	NaN	Basidiosporas	7878	5051	-36
Helicomina	48	80	67	Erysiphe/Oidium	0	48	NaN	Cladosporium	1462	271	-81
				Fusarium	16	0	NaN	Chaetomium	0	16	0
				Ganoderma	302	207	-32	Coprinus/Agaricus	128	128	0
				Leptosphaeria-Like	32	48	50	Diatrypaceae	2034	1938	-5
				Periconia	16	16	0	Smut/Myxomycete	16	64	300
				Pithomyces	16	64	300				
				Pleospora	64	16	-75				
				Nigrospora	32	32	0				
				Rusts Puccinia	32	64	100				
				Periconia	16	16	0				
				Spegazzinia	0	16	NaN				
				Ulocladium	16	16	0				
				Tetrapyrgos	0	16	NaN				

656

Regarding the analysis of bi-hourly pollen concentration (Figure 15) it can be observed that days with AD presented the highest pollen concentrations from 2000 to 2400 UTC, which suggests pollen transport from emission sources far away from the monitoring station. In addition, airborne fungal spore taxa did not show significant concentrations during these days. The spore taxa identified during the selected period were Cladosporium, Alternaria, Pleospora, Tilletia and Leptosphaeria.

661

662



663

Figure 15 Bi-hourly values of total pollen concentration recorded by Hirst trap for the selected period in León. Days without AD inundation (\bullet), Days with AD inundation (\bullet).

664

665

666

667

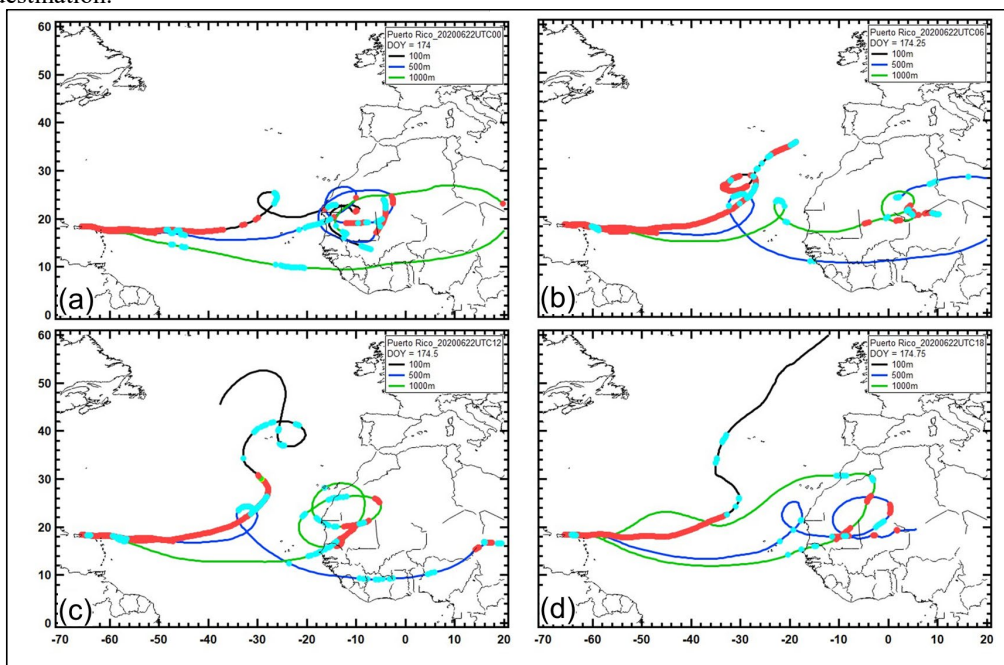


668 **3.4 Back Trajectory Analysis**

669

670 The origins and histories of the air masses were evaluated using the National Oceanic and
671 Atmospheric Administration (NOAA) Hybrid Single-Particle Lagrangian Integrated Trajectory
672 model (HYSPLIT) back trajectory model, incorporating the Global Data Assimilation System
673 (GDAS) with one degree resolution (Stein et al., 2015; Rolph et al. 2017). The model was run for
674 thirteen and five days for PR and León, respectively, time periods commensurate with the number of
675 days between when dust was seen in the satellite data to originate over northern Africa and arrive at
676 the two destinations, respectively. The ending altitudes were chosen to be 100, 500 and 1000 m based
677 on previous studies that have shown that the AD layers can range in thickness between 100 and 1000
678 m (Ramírez-Romero et al., 2021). Figure 16 shows representative back trajectories for PR on June
679 22, 2020, color coded by altitude and with markers (red) that indicate when and where the air was
680 within the mixed layer and when the air mass encountered precipitation (light blue markers). These
681 mixed layer parameters were selected to show where the originating air might have first picked up
682 the dust and then later where the air might have interacted with other sources of aerosols, e.g. marine
683 aerosols when passing over the Atlantic Ocean. The precipitation is added because it can contribute
684 to cloud processing of aerosols and potential removal of particles before the air arrives at its
685 destination.

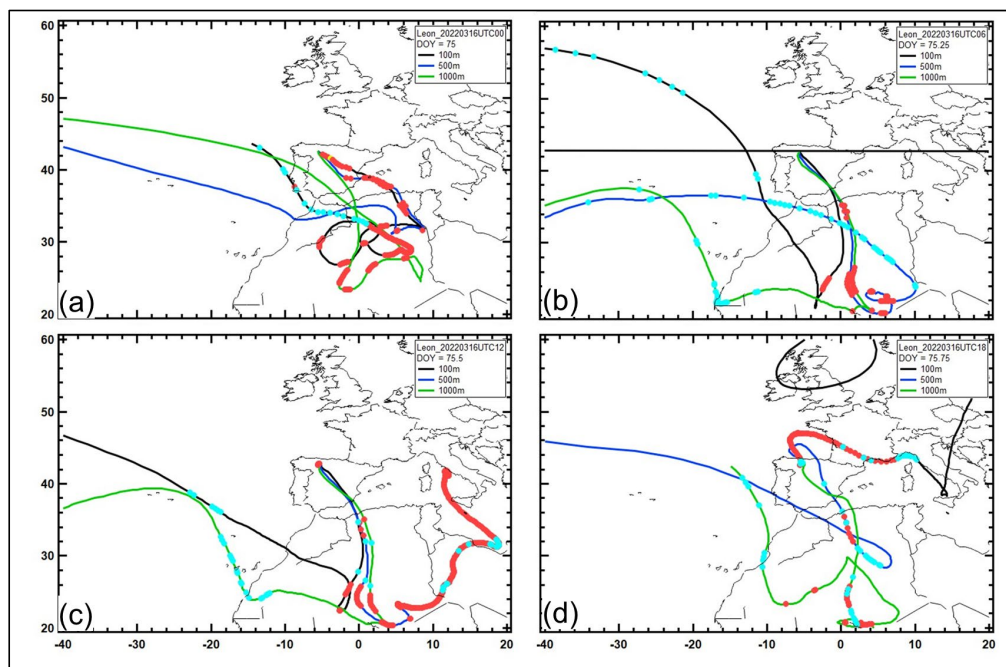
686



687 **Figure 16. Thirteen day back trajectories of air masses arriving at 100 m (black curve), 500 m (blue curve) and 1000**
688 **m (green curve) over Puerto Rico. The red markers show every hour the air was in the mixed layer and the light blue**
689 **markers denote each hour where rain was encountered. These are from June 22, 2020 at (a) 0000 UTC, (b) 0600 UTC,**
690 **(c) 1200 UTC and (d) 1800 UTC.**



691



692 *Figure 17. The same as Fig. 16 but for five day back trajectories of air masses arriving over León on March 16, 2022*
693 *at (a) 0000 UTC, (b) 0600 UTC, (c) 1200 UTC and (d) 1800 UTC.*

694

695 Over the 24-hour period that AD was arriving on June 22nd, at UTC 0000, 0600, 1200 and 1800 (Figs.
696 16a-d) the air can be seen originating from over the African Sahara and Sahel. At UTC 0000 all three
697 trajectories had been over this region and the red markers also show that they had been there in the
698 mixed layer at different times, confirming that particles indigenous to that region would have
699 originated there. At 0600, 1200 and 1800 UTC the 100, 500 and 1000 m trajectories do not always
700 indicate being in the mixed layer, but at least one of them does; hence, the AD continues to be
701 transported to PR over these time periods. It is also important to note that the 100 m trajectory, as
702 well as sometimes the 500 m trajectory, arrive over PR after traveling several hundred kilometers (>
703 24 hrs) in the mixed layer. With respect to cloud processing the HYSPLIT model indicates that
704 throughout the day the air had encountered precipitation first over Africa and then on its travel over
705 the Atlantic Ocean before arriving in PR.

706

707 Figure 17 provides the same information for León over four five-hour time periods on March 16,
708 2022. Similar to what was observed with the air masses that brought AD to PR, the air masses that
709 arrived over León at 100, 500 and 1000 m had all been in the mixed layer in northern Africa for
710 varying lengths of time. Whereas most of the AD that arrived over PR originated in western Africa,
711 those air masses over León were bringing particles from regions in northern and northeastern Africa.
712 Much of the air, particularly that which arrived at 500 m over León, had also encountered frequent
713 periods of precipitation as indicated by the model.

714

715 4.0 Discussion

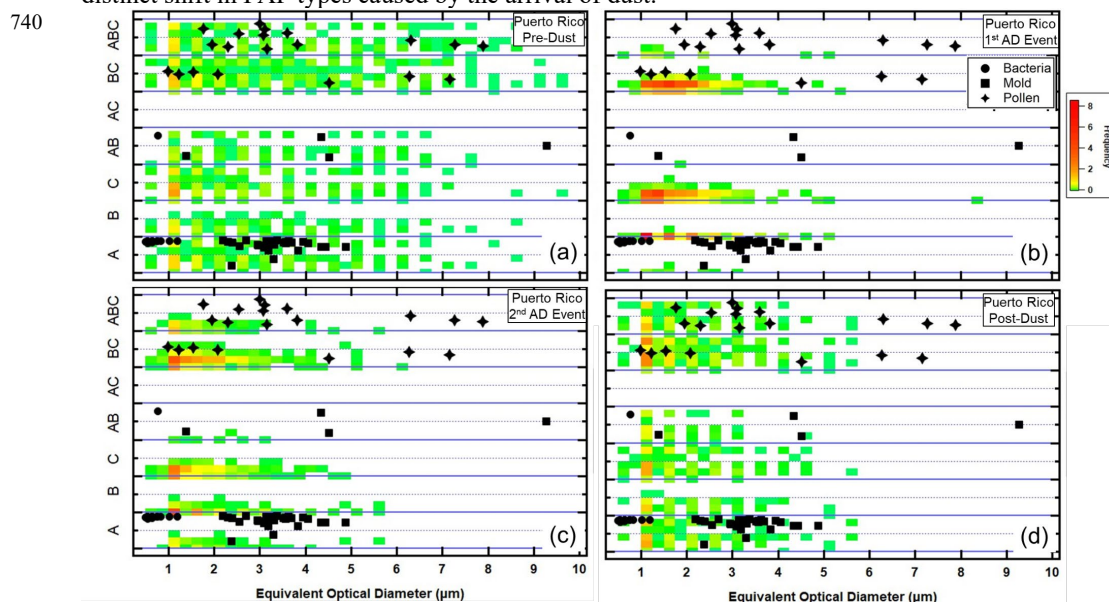
716

717 In Section 2.3.3 we posed questions related to how the WIBS measurements could be used to
718 distinguish differences in bioaerosol taxa in the background FAP of PR and León and between
719 background and dust events. Although the size distributions of the number concentrations and
720 intensities of the FAP Types in PR and León cannot be used to speciate bioaerosols, the distinct
721 differences in the relative fraction of total FAP in smaller and larger particles indicate that the



722 mixtures of BSP types, i.e., bacteria, mold or pollen, are clearly dissimilar. This is observed when
723 comparing the two regional background aerosols and when comparing the changes when AD arrives.
724

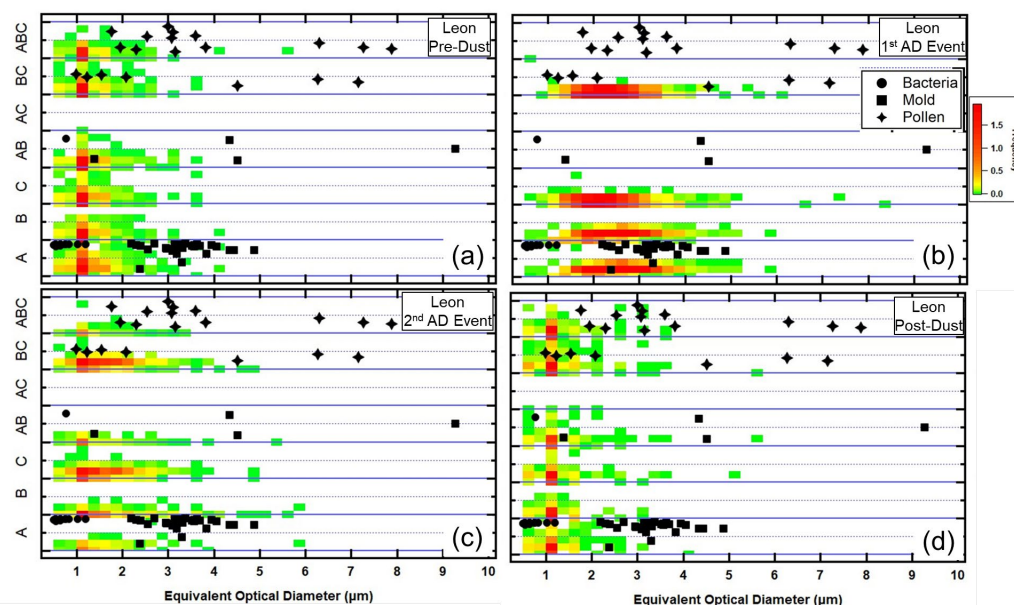
725 The contrasts in FAP properties are highlighted by placing their physical and fluorescing properties
726 in the context of these same properties generated using laboratory studies, as was demonstrated in
727 Fig. 2. Figures 18 and 19 summarize the FAP properties for the PR and León regions, before, during
728 and after dust events as they compare to the FAP properties of bacteria, mold and pollen measured in
729 the laboratory. A cursory examination of these two figures confirms that the FAP properties are
730 significantly different between PR and León, without and with dust. While this result should not be
731 considered surprising, displaying the FAP properties as illustrated in these figures offers a way to
732 indirectly compare the ambient FAP properties with those of actual BSPs. The distribution of FAP in
733 the PR background aerosol (Figs. 18a and d) corresponds mostly to the laboratory mold and pollen
734 with only a small fraction falling into the bacteria type and size. The PR FAP that falls in the pollen
735 region is mostly in EODs < 5 μm . There is a population of FAP types B, C and AB that are found in
736 the ambient environment but have no corresponding laboratory BSP types that they can be associated
737 with. With the arrival of the dust, the FAP maps shift significantly with the largest majority of the
738 fluorescing particles appearing in the Type B, C and BC categories and at EODs < 5 μm . This is a
739 distinct shift in FAP types caused by the arrival of dust.



741 *Figure 18. Similar to Fig. 2. Except the laboratory BSP maps are combined with the frequency of occurrence (color*
742 *coded) of FAP types. The color scale denotes how frequently during the two day periods the FAP types and EODs fell*
743 *within the different regions. (a) Puerto Rico two days before the AD event, (b) and (c) Puerto Rico during the 1st*
744 *and 2nd AD events and (d) Puerto Rico after the AD event.*
745



746



747 *Figure 19. The same as Fig. 18, except for measurements in León.*

748

749

750

751

752

753

754

755

756

757

758

759

760

761

762

763

764

765

766

767

768

769

770

771

772

773

774

775

776

777

778

The FAP patterns in the León aerosols are shown in Fig. 19 and suggest that the largest number of background aerosols should be considered bacteria-like and small, pollen-like as compared to the laboratory BSPs. The highest frequencies are found at EODs < 2 μm, evenly distributed over all FAP types except Type AC. This suggests that many of the FAP measured in León are different from the laboratory BSP taxa. The arrival of the dust dramatically shifts the pattern of the FAP – the highest frequencies are now in Types A, B, C and AC and the EODs are now centered between 4 μm and 6 μm during the first AD event. These sizes decrease during the 2nd AD event before returning to mostly < 2 μm in the post-dust time period. These results suggest that the background FAPs are mostly bacteria and pollen, similar to the background air, with some fraction with FAP types that do not correspond to the taxa of the BSPs tested in the one laboratory study. The dust brings in bioaerosols whose FAP properties include those that are similar to bacteria, mold and pollen, but now with larger EODs.

The results shown in Figs. 18 and 19 offer compelling evidence that the WIBS measurements distinguish between types and compositions of bioaerosols and that the no-dust and dust cases can be clearly separated, as can the background populations of PR and León. What about information on how FAP are physically mixed with non-FAP aerosol? To address this question, we remind the reader what the differences between internally and externally mixed aerosol ensembles are. Figure S8 is a conceptual diagram that compares internally and externally aerosols. In short, we do not expect to have only one or the other type of situation given that turbulent mixing will lead to the eventual combination of the two. Nevertheless, there are several reasons to expect that one or the other might dominate, depending upon the age of the air masses and the types of physical processes that can occur between the origin of the dust plume and when it arrives several hours or days later in PR and León.

Referring back to Fig. 10a we observe a clear difference between PR and León when comparing the changes in the MEODs, over all FAP types, when dust arrives. The MEODs *decrease* by 20-30% in PR and *increase* by 30-50% in León. These opposite changes were also seen in the size distributions shown in Figs. 8 and 9, i.e., in general, FAP concentrations in sizes <5 μm increased in PR and decreased in León. These differences can be explained, to some degree, by differences in the mixing state of FAP and dust during AD events. The large decrease in the FAP MEOD in PR suggests that



779 the dust is bringing many more small FAPs than are found in the background; however, the increase
780 in the larger FAPs indicates that some of these FAP are also internally mixed with the larger dust
781 particles. Hence, the PR dust may be more externally than internally mixed (Fig. S8a). On the other
782 hand, the AD event in León increased the MEODs over all the sizes; however, the larger particles (>5
783 μm) increased proportionately more than those $<5 \mu\text{m}$. This leads to the conclusion that the FAP in
784 the León AD event are more internally mixed, i.e., that a large fraction of the AD FAP are attached
785 to or mixed with the AD, as illustrated in Fig. S8b.

786
787 If we assume that the AD that arrives in PR and León originated through similar processes over
788 northern Africa, whereby dust and FAP are lofted from the surface, then the differences that are
789 observed in the FAP properties when they arrive in León and PR are likely a result of the
790 transformations that occurred during their transport. The three primary processes that lead to these
791 transformations are coagulation, sedimentation and precipitation. The AD had traveled over much
792 longer distances and time before reaching PR than when arriving over León. The back trajectory
793 analyses showed that these air masses had also traveled many hours in the boundary layer prior to
794 reaching PR. Some of the FAP are likely attached to dust particles when they are lifted from the
795 surface at their origin, while others will collide with the dust during transport as a result of small scale
796 turbulent eddies, and sedimentation of the larger dust particles falling through the smaller FAP.
797 Electrical charging of the particles, leading to further coagulation cannot be discounted. Particles with
798 an aerodynamic diameter of $1 \mu\text{m}$ and a density of 2 g cm^{-3} fall at a speed of 6 m/day while a $10 \mu\text{m}$
799 particle falls at 500 m/day ; hence, the particles $\geq 10 \mu\text{m}$ will fall 2.5 km and 6.5 km during their 5
800 and 13 day travel from Africa to León and PR, respectively. This type of removal of the larger
801 particles, while smaller particles remain aloft, can explain the difference between PR and León
802 mixtures of FAP and dust. Not only did the particles in the AD air masses that arrived in PR have
803 three times longer to fall than those in León, but the back trajectory analysis also revealed that the air
804 arriving in PR had been in the mixed layer many more hours than the air masses reaching León.
805 Traveling in this layer would place the particles much closer to the surface and have a shorter distance
806 to sediment and be removed.

807 808 **5.0 Data availability**

809
810 The WIBS data and complementary aerosol measurements described in this manuscript can be
811 accessed at the Zenodo repository, under [DOI .10.5281/zenodo.10680977](https://doi.org/10.5281/zenodo.10680977) (Baumgardner, 2024)

812 813 **6.0 Summary and Conclusions**

814
815 Two major African dust events, one over the island of Puerto Rico and the other over the city of León,
816 Spain have been analyzed, the former in June, 2020 and the latter in March, 2022. From measurements
817 with two Wideband Integrated Bioaerosol Spectrometers (WIBS) and complementary aerosol data
818 we make the following observations and conclusions:

- 819
820 1. The intrusion of dust over the Caribbean and Iberian Peninsula leads to a significant impact
821 on the size distributions and composition of the local populations of aerosols.
- 822 2. Differences in the FAP sizes and fluorescing properties, prior to the AD events, are clearly
823 seen in comparisons between the background aerosol populations in PR and León.
- 824 3. The arrival of AD over the two regions significantly alters the properties of the local aerosol
825 populations as observed in the WIBS and PM measurements. The magnitude of these altered
826 properties are different at the two locations, differences attributed to the age of the AD air
827 masses, five and 13 days old, when arriving in León and PR, respectively.
- 828 4. As deduced from changes in the shapes of the FAP size distributions, with the intrusion of the
829 AD the FAP is both internally and externally mixed with other non-FAP particles in the dust



830 plume; however, the AD that arrives in PR appears to have a much higher proportion of
831 externally mixed FAP than León.

832 5. The comparison of the maps of relative frequency of FAP Types and their average EOD,
833 juxtaposed with laboratory bacteria, mold and pollen, indicates that the mixtures of FAP and
834 dust in PR are significantly different than those in León. The AD dust over PR clustered most
835 in FAP types C and BC while in León the primary AD types were A, B, C and AC. When
836 compared with the laboratory FAP, Type A is related to bacteria and BC to pollen. Types B
837 and C were not common in the laboratory measurements used in this study (Hernandez et al.,
838 2016) nor did other similar laboratory studies, e.g., Savage et al. (2017), have these types of
839 FAP.

840

841 The analysis approach that has been introduced in this study highlights the importance of using
842 metrics that focus on relative changes in the number concentration and fluorescence intensity size
843 distributions of the seven types of FAP. The median equivalent optical diameter (MEOD) is a
844 sensitive metric that can quantitatively document these changes along with maps of the frequency of
845 FAP type versus EOD that highlight how the FAP types in AD are significantly different from
846 background FAP in PR or León.

847

848 These two data sets will be a useful contribution to the larger data bases of African and Asian dust
849 aerosols that have been transported large distances and that may be carrying bioaerosols, some which
850 may be similar to those found in the local regions inundated by this dust while other might be more
851 damaging to the environments where they eventually are deposited or inhaled.

852

853 **7.0 Competing Interests**

854

855 The contact author has declared that none of the authors has any competing interests.

856

857 **8.0 Acknowledgements**

858

859 The authors gratefully acknowledge the NOAA Air Resources Laboratory (ARL) for the provision
860 of the HYSPLIT transport and dispersion model and/or READY website
861 (<https://www.ready.noaa.gov>) used in this publication. This work was partially supported by the Junta
862 de Castilla y Leon co-financed with European FEDER funds (Grant LE025P20), by the
863 AEROHEALTH project (Ministry of Science and Innovation, co-financed with European FEDER
864 funds. Grant PID2019-106164RBI00) and by National Science Foundation-MRI grant (1829297).
865 Furthermore, it is part of the project TED2021-132292B-I00, funded by
866 MCIN/AEI/10.13039/501100011033 and by the European Union “NextGenerationEU”/PRTR.

867

868 **9.0 Author contributions**

869

870 B. Sarangi and B. Bolaños-Rosero provided all the data from the Puerto Rico site, A. Calvo and R.
871 Fraile provided the WBS and FM-120 measurements from the León, Spain measurement site. D.
872 Baumgardner and D. Hughes assisted in the processing of WBS measurements from PR and León,
873 A. Rodríguez-Fernández and D. Fernández-González provided the Hirst sampler data from León, C.
874 Blanco-Alegre, C. Gonçalves and E. D. Vicente operated the WBS and FM-120 during the León
875 project, O. L. Mayol Bracero helped to edit the manuscript and M. Hernandez contributed the
876 laboratory studies of FAP.

877

878 **10.0 References**

879 Alastuey, A., Querol, X., Aas, W., Lucarelli, F., Pérez, N., Moreno, T., Cavalli, F., Areskou, H.,
880 Balan, V., Catrambone, M., Ceburnis, D., Cerro, J. C., Conil, S., Gevorgyan, L., Hueglin, C., Imre,



- 881 K., Jaffrezo, J.-L., Leeson, S. R., Mihalopoulos, N., Mitosinkova, M., O'Dowd, C. D., Pey, J., Putaud,
882 J.-P., Riffault, V., Ripoll, A., Sciare, J., Sellegri, K., Spindler, G., and Yttri, K. E.: Geochemistry of
883 PM10 over Europe during the EMEP intensive measurement periods in summer 2012 and winter
884 2013, *Atmos. Chem. Phys.*, 16, 6107–6129, <https://doi.org/10.5194/acp-16-6107-2016>, 2016.
- 885 Allan, J., D. Baumgardner, G.B. Raga., O. L. Mayol-Bracero, F. Morales-García, F. García-García,
886 G. Montero-Martínez, S. Borrmann, J. Schneider, S. Mertes, S. Walter, M. Gysel, U. Dusek, G. P.
887 Frank, and M. Kraemer, 2008: Clouds and Aerosols in Puerto Rico – a new Evaluation, *Atmos. Chem.*
888 *Phys.*, 8, 1293–1309, <https://doi.org/10.5194/acp-8-1293-2008>, 2008.
- 889 Andrews, E., Sheridan, P. J., Ogren, J. A., Hageman, D., Jefferson, A., Wendell, J., Alástuey, A.,
890 Alados-Arboledas, L., Bergin, M., Ealo, M., Gannet Hallar, A., Hoffer, A., Kalapov, I., Keywood,
891 M., Kim, J., Kim, S. W., Kolonjari, F., Labuschagne, C., Lin, N. H., Macdonald, A., Mayol-Bracero,
892 O. L., McCubbin, I. B., Pandolfi, M., Reisen, F., Sharma, S., Sherman, J. P., Sorribas, M., and Sun,
893 J.: Overview of the NOAA/ESRL federated aerosol network, *Bull Am Meteorol Soc*, 100(1), 123–
894 135, <https://doi.org/10.1175/BAMS-D-17-0175.1>, 2019.
- 895 Anees-Hill, S., Douglas, P., Pashley, C. H., Hansell, A., and Marczyklo, E. L.: A systematic review of
896 outdoor airborne fungal spore seasonality across Europe and the implications for health, 818, 151716,
897 <https://doi.org/10.1016/j.scitotenv.2021.151716>, 2022.
- 898 Asutosh, A., Vinoj, V., Murukesh, N., Ramisetty, R., and Mittal, N.: Investigation of June 2020 giant
899 Saharan dust storm using remote sensing observations and model reanalysis, *Sci Rep*, 12, 6114,
900 <https://doi.org/10.1038/s41598-022-10017-1>, 2022.
- 901 Baumgardner, D.: African Dust with Bioaerosols data repository, [DOI .10.5281/zenodo.10680977](https://doi.org/10.5281/zenodo.10680977),
902 [2024](https://doi.org/10.5281/zenodo.10680977).
- 903 Calvo, A. I., Baumgardner, D., Castro, A., Fernández-González, D., Vega-Maray, A. M., Valencia-
904 Barrera, R. M., Oduber, F., Blanco-Alegre, C., and Fraile, R.: Daily behavior of urban Fluorescing
905 Aerosol Particles in northwest Spain, 184, 262–277, *Atmos Environ*,
906 <https://doi.org/10.1016/j.atmosenv.2018.04.027>, 2018.
- 907 Choël, M., Ivanovsky, A., Roose, A., Hamzé, M., Blanchenet, A. M., and Visez, N.: Quantitative
908 assessment of coagulation of atmospheric particles onto airborne birch pollen grains, *J Aerosol Sci*,
909 161, 105944, <https://doi.org/10.1016/j.jaerosci.2021.105944>, 2022.
- 910 Crawford, I., Ruske, S., Topping, D. O., and Gallagher, M. W.: Evaluation of hierarchical
911 agglomerative cluster analysis methods for discrimination of primary biological aerosol, *Atmos Meas*
912 *Tech*, 8, 4979–4991, <https://doi.org/10.5194/amt-8-4979-2015>, 2015.
- 913 Després, V. R., Alex Huffman, J., Burrows, S. M., Hoose, C., Safatov, A. S., Buryak, G., Fröhlich-
914 Nowoisky, J., Elbert, W., Andreae, M. O., Pöschl, U., and Jaenicke, R.: Primary biological aerosol
915 particles in the atmosphere: A review, 64, 15598, <https://doi.org/10.3402/tellusb.v64i0.15598>, 2012.
- 916 Díaz, J., Linares, C., Carmona, R., Russo, A., Ortiz, C., Salvador, P., and Trigo, R. M.: Saharan dust
917 intrusions in Spain: Health impacts and associated synoptic conditions, *Environ Res*, 156, 455–467,
918 <https://doi.org/10.1016/j.envres.2017.03.047>, 2017.
- 919 Dietzel, K., Valle, D., Fierer, N., U'ren, J. M., and Barberán, A.: Geographical distribution of fungal
920 plant pathogens in dust across the United States, *Front Ecol Evol*, 7, 1–8,
921 <https://doi.org/10.3389/fevo.2019.00304>, 2019.



- 922 Escudero M., Castillo S., Querol X., Avila A., Alarcón M., Viana M.M., Alastuey A., Cuevas E.,
923 Rodríguez S.: Wet and dry African dust episodes over Eastern Spain, *J. Geophys. Res.*, 110, D18S08,
924 2005.
- 925 Escudero, M., Querol, X., Ávila, A., and Cuevas, E.: Origin of the exceedances of the European daily
926 PM limit value in regional background areas of Spain, *Atmos Environ*, 41, 730–744,
927 <https://doi.org/10.1016/j.atmosenv.2006.09.014>, 2007.
- 928 Feofilova, E. P.: The fungal cell wall: Modern concepts of its composition and biological function,
929 *79(6)*, 711–720, <https://doi.org/10.1134/S0026261710060019>, 2010.
- 930 Francis, D., Fonseca, R., Nelli, N., Cuesta, J., Weston, M., Evan, A., and Temimi, M.: The
931 Atmospheric Drivers of the Major Saharan Dust Storm in June 2020, *47*, e2020GL090102,
932 <https://doi.org/10.1029/2020GL090102>, 2020.
- 933 Fröhlich-Nowoisky, J., Pickersgill, D. A., Després, V. R., and Pöschl, U.: High diversity of fungi in
934 air particulate matter, *Proc Natl Acad Sci U S A*, 106(31), 12814–12819,
935 <https://doi.org/10.1073/pnas.0811003106>, 2009.
- 936 Fröhlich-Nowoisky, J., Kampf, C. J., Weber, B., Huffman, J. A., Pöhlker, C., Andreae, M. O., Lang-
937 Yona, N., Burrows, S. M., Gunthe, S. S., Elbert, W., Su, H., Hoor, P., Thines, E., Hoffmann, T.,
938 Després, V. R., and Pöschl, U.: Bioaerosols in the Earth system: Climate, health, and ecosystem
939 interactions, 346–376, <https://doi.org/10.1016/j.atmosres.2016.07.018>, 2016.
- 940 Gabey, A. M., Vaitilingom, M., Freney, E., Boulon, J., Sellegri, K., Gallagher, M. W., Crawford, I.
941 P., Robinson, N. H., Stanley, W. R., and Kaye, P. H.: Observations of fluorescent and biological
942 aerosol at a high-altitude site in central France, *Atmos. Chem. Phys.*, 13, 7415–7428,
943 <https://doi.org/10.5194/acp13-7415-2013>, 2013.
- 944 Grinn-Gofroñ, A., Nowosad, J., Bosiacka, B., Camacho, I., Pashley, C., Belmonte, J., De Linares, C.,
945 Ianovici, N., Manzano, J. M. M., Sadyś, M., Skjøth, C., Rodinkova, V., Tormo-Molina, R., Vokou,
946 D., Fernández-Rodríguez, S., and Damialis, A.: Airborne *Alternaria* and *Cladosporium* fungal spores
947 in Europe: Forecasting possibilities and relationships with meteorological parameters, *Science of the*
948 *Total Environment*, 653, 938–946, <https://doi.org/10.1016/j.scitotenv.2018.10.419>, 2019.
- 949 Hallegraeff G, Coman F, Davies C, Hayashi A, McLeod D, Slotwinski A, Whittock L, Richardson
950 AJ. Australian dust storm associated with extensive *Aspergillus sydowii* fungal “bloom” in coastal
951 waters. *Applied and environmental microbiology*, 80(11), 3315-
952 3320, <https://doi.org/10.1128/AEM.04118-13> 2014.
- 953 Hannan, P. J.: Electrophoretic properties of spores of *Aspergillus niger*., *Appl Microbiol*, 9, 113–117,
954 <https://doi.org/10.1128/aem.9.2.113-117.1961>, 1961.
- 955 Hernandez, M., Perring, A.E., McCabe, K., Kok, G., Granger, G., Baumgardner, D.: Chamber
956 catalogues of optical and fluorescent signatures distinguish bioaerosol classes. *Atmos. Meas. Tech* 9,
957 3283–3292, <https://doi.org/10.5194/amt-9-3283-2016>, 2016.
- 958 Hirst, J. M.: An automatic volumetric spore trap, *Annals of Applied Biology*, 39,
959 <https://doi.org/10.1111/j.1744-7348.1952.tb00904.x>, 1952.
- 960 Holben, B. N., Eck, T. F., Slutsker, I., Tanré, D., Buis, J. P., Setzer, A., Vermote, E., Reagan, J. A.,
961 Kaufman, Y. J., Nakajima, T., Lavenu, F., Jankowiak, I., and Smirnov, A.: AERONET—A Federated



- 962 Instrument Network and Data Archive for Aerosol Characterization, Remote Sensing of
963 Environment, 66, 1-16, [https://doi.org/10.1016/S0034-4257\(98\)00031-5](https://doi.org/10.1016/S0034-4257(98)00031-5), 1998.
- 964 Huffman, J. A., Prenni, A. J., Demott, P. J., Pöhlker, C., Mason, R. H., Robinson, N. H., Fröhlich-
965 Nowoisky, J., Tobo, Y., Després, V. R., Garcia, E., Gochis, D. J., Harris, E., Müller-Germann, I.,
966 Ruzene, C., Schmer, B., Sinha, B., Day, D. A., Andreae, M. O., Jimenez, J. L., Gallagher, M.,
967 Kreidenweis, S. M., Bertram, A. K., and Pöschl, U.: High concentrations of biological aerosol
968 particles and ice nuclei during and after rain, *Atmos Chem Phys*, 13, 6151–6164,
969 <https://doi.org/10.5194/acp-13-6151-2013>, 2013.
- 970 Kasprzyk, I., Rodinkova, V., Šaulienė, I., Ritenberga, O., Grinn-Gofron, A., Nowak, M., Sulborska,
971 A., Kaczmarek, J., Weryszko-Chmielewska, E., Bilous, E., and Jedryczka, M.: Air pollution by
972 allergenic spores of the genus *Alternaria* in the air of central and eastern Europe, *Environmental
973 Science and Pollution Research*, 22, 9260–9274, <https://doi.org/10.1007/s11356-014-4070-6>, 2015.
- 974 Kaye, P. H., Stanley, W. R., Hirst, E., Foot, E. V., Baxter, K. L., and Barrington, S. J.: Single particle
975 multichannel bio-aerosol fluorescence sensor, *Opt Express*, 13, 3583-3593,
976 <https://doi.org/10.1364/opex.13.003583>, 2005.
- 977 Lakowicz, J. R.: Principles of fluorescence spectroscopy, <https://doi.org/10.1007/978-0-387-46312-4>, 2006.
- 979 Lawler, M. J., Draper, D. C., and Smith, J. N.: Atmospheric fungal nanoparticle bursts, *Sci Adv*, 6,
980 <https://doi.org/10.1126/sciadv.aax9051>, 2020.
- 981 Leach, C. M.: An electrostatic theory to explain violent spore liberation by *Drechslera turcica* and
982 other fungi., *Mycologia*, 68, 63-86, <https://doi.org/10.2307/3758898>, 1976.
- 983 Lyamani, H., Valenzuela, A., Perez-Ramirez, D., Toledano, C., Granados-Muñoz, M. J., Olmo, F. J.,
984 and Alados-Arboledas, L.: Aerosol properties over the western Mediterranean basin: temporal and
985 spatial variability, *Atmos. Chem. Phys.*, 15, 2473–2486, <https://doi.org/10.5194/acp-15-2473-2015>,
986 2015.
- 987 Mayol-Bracero, O. L., Rosario, O., Corrigan, C. E., Morales, R., Torres, I., and Pérez, V.: Chemical
988 characterization of submicron organic aerosols in the tropical trade winds of the caribbean using gas
989 chromatography/mass spectrometry, *Atmos Environ*, 35, 1735-1745, [https://doi.org/10.1016/S1352-2310\(00\)00524-0](https://doi.org/10.1016/S1352-2310(00)00524-0), 2001.
- 991 Morrison, D., Crawford, I., Marsden, N., Flynn, M., Read, K., Neves, L., Foot, V., Kaye, P., Stanley,
992 W., Coe, H., Topping, D., and Gallagher, M.: Quantifying bioaerosol concentrations in dust clouds
993 through online UV-LIF and mass spectrometry measurements at the Cape Verde Atmospheric
994 Observatory, *Atmos Chem Phys*, 20, 14473–14490, <https://doi.org/10.5194/acp-20-14473-2020>,
995 2020.
- 996 Novakov, T., Corrigan, C. E., Penner, J. E., Chuang, C. C., Rosario, O., and Mayol Bracero, O. L.:
997 Organic aerosols in the Caribbean trade winds: A natural source?, *Journal of Geophysical Research
998 Atmospheres*, 102, 21307-21313, <https://doi.org/10.1029/97jd01487>, 1997.
- 999 Perring, A. E., Schwarz, J. P., Baumgardner, D., Hernandez, M. T., Spracklen, D. V., Heald, C. L.,
1000 Gao, R. S., Kok, G., McMeeking, G. R., McQuaid, J. B., and Fahey, D. W.: Airborne observations of
1001 regional variation in fluorescent aerosol across the United States, *J. Geophys. Res.-Atmos.*, 120,
1002 1153–1170, <https://doi.org/10.1002/2014JD022495>, 2015.



- 1003 Pöhlker, C., Huffman, J. A., and Pöschl, U.: Autofluorescence of atmospheric bioaerosols –
1004 fluorescent biomolecules and potential interferences, *Atmos. Meas. Tech.*, 5, 37–71,
1005 <https://doi.org/10.5194/amt-5-37-2012>, 2012.
- 1006 Prospero, J. M., Collard, F. X., Molinié, J., and Jeannot, A.: Characterizing the annual cycle of
1007 African dust transport to the Caribbean Basin and South America and its impact on the environment
1008 and air quality, *Global Biogeochem Cycles*, 28(7), 757–773, <https://doi.org/10.1002/2013GB004802>,
1009 2014.
- 1010 Pu, B. and Jin, Q.: A record-breaking trans-Atlantic African dust plume associated with atmospheric
1011 circulation extremes in June 2020, *Bull Am Meteorol Soc*, 102(7), E1340–E1356,
1012 <https://doi.org/10.1175/BAMS-D-21-0014.1>, 2021.
- 1013 Pulimood, T. B., Corden, J. M., Bryden, C., Sharples, L., and Nasser, S. M.: Epidemic asthma and
1014 the role of the fungal mold *Alternaria alternata*, *Journal of Allergy and Clinical Immunology*, 120 (3),
1015 610–617, <https://doi.org/10.1016/j.jaci.2007.04.045>, 2007.
- 1016 Querol, X., Alastuey, A., Pandolfi, M., Reche, C., Pérez, N., Minguillón, M. C., Moreno, T., Viana,
1017 M., Escudero, M., Orío, A., Pallarés, M., and Reina, F.: 2001–2012 trends on air quality in Spain,
1018 *Science of the Total Environment*, 490, 957–969, <https://doi.org/10.1016/j.scitotenv.2014.05.074>,
1019 2014.
- 1020 Ramírez-Romero, C., Jaramillo, A., Córdoba, M. F., Raga, G. B., Miranda, J., Alvarez-Ospina, H.,
1021 Rosas, D., Amador, T., Kim, J. S., Yakobi-Hancock, J., Baumgardner, D., and Ladino, L. A.: African
1022 dust particles over the western Caribbean – Part I: Impact on air quality over the Yucatán Peninsula,
1023 *Atmos. Chem. Phys.*, 21, 239–253, <https://doi.org/10.5194/acp-21-239-2021>, 2021.
- 1024 Robinson, N. H., Allan, J. D., Huffman, J. A., Kaye, P. H., Foot, V. E., and Gallagher, M.: Cluster
1025 analysis of WIBS single-particle bioaerosol data, *Atmos Meas Tech*, 6, 337–347,
1026 <https://doi.org/10.5194/amt-6-337-2013>, 2013.
- 1027 Rodríguez-Arias, R. M., Rojo, J., Fernández-González, F., and Pérez-Badia, R.: Desert dust intrusions
1028 and their incidence on airborne biological content. Review and case study in the Iberian Peninsula,
1029 *Environmental Pollution*, 316, 120464, <https://doi.org/10.1016/j.envpol.2022.120464>, 2023.
- 1030 Rodríguez-Fernández, A., Blanco-Alegre, C., Vega-Maray, A. M., Valencia-Barrera, R. M., Molnár,
1031 T., and Fernández-González, D.: Effect of prevailing winds and land use on *Alternaria* airborne spore
1032 load, *J Environ Manage*, 332, 117414, <https://doi.org/10.1016/j.jenvman.2023.117414>, 2023.
- 1033 Rodríguez, S., Querol, X., Alastuey, A., Kallos, G., and Kakaliagou, O.: Saharan dust contributions
1034 to PM10 and TSP levels in Southern and Eastern Spain, *Atmos Environ*, 35 (14), 2433–2447,
1035 [https://doi.org/10.1016/S1352-2310\(00\)00496-9](https://doi.org/10.1016/S1352-2310(00)00496-9), 2001.
- 1036 Rolph, G., Stein, A., and Stunder, B.: Real-time Environmental Applications and Display sYstem:
1037 READY, Environmental Modelling and Software, 95, 210–228,
1038 <https://doi.org/10.1016/j.envsoft.2017.06.025>, 2017.
- 1039 Ryder, C. L., Highwood, E. J., Walser, A., Seibert, P., Philipp, A., and Weinzierl, B.: Coarse and
1040 giant particles are ubiquitous in Saharan dust export regions and are radiatively significant over the
1041 Sahara, *Atmos Chem Phys*, 19, 15353–15376, <https://doi.org/10.5194/acp-19-15353-2019>, 2019.
- 1042 Salvador, P., Artíñano, B., Molero, M., Viana, M., Pey, J., Alastuey, A., and Querol, X.: African dust
1043 contribution to ambient aerosol levels across central Spain: Characterization of long-range transport



- 1044 episodes of desert dust, *Atmos. Res.*, 127, 117–129, <https://doi.org/10.1016/j.atmosres.2011.12.011>,
1045 2013.
- 1046 Sarangi, B., Baumgardner, D., Bolaños-Rosero, B., and Mayol-Bracero, O. L.: Measurement report:
1047 An exploratory study of fluorescence and cloud condensation nuclei activity of urban aerosols in San
1048 Juan, Puerto Rico, *Atmos. Chem. Phys.*, 22, 9647–9661, <https://doi.org/10.5194/acp-22-9647-2022>,
1049 2022.
- 1050 Savage, N., Krentz, C., Könemann, T., Han, T.T., Mainelis, G., Pöhlker, C., Huffman, J.A.:
1051 Systematic characterization and fluorescence threshold strategies for the Wideband integrated
1052 bioaerosol sensor (WIBS) using size-resolved biological and interfering particles. *Atmos. Meas.*
1053 *Tech. Discuss* 10, 4279–4302. <https://doi.org/10.5194/amt-2017-170>, 2017.
- 1054 Sénéchal, H., Visez, N., Charpin, D., Shahali, Y., Peltre, G., Biolley, J. P., Lhuissier, F., Couderc, R.,
1055 Yamada, O., Malrat-Domenge, A., Pham-Thi, N., Poncet, P., and Sutra, J. P.: A review of the effects
1056 of major atmospheric pollutants on pollen grains, pollen content, and allergenicity,
1057 *ScientificWorldJournal*, 940243, <https://doi.org/10.1155/2015/940243>, 2015.
- 1058 Shinn, E. A., Smith, G. W., Prospero, J. M., Betzer, P., Hayes, M. L., Garrison, V., and Barber, R.
1059 T.: African dust and the demise of Caribbean coral reefs, *Geophys Res Lett*, 27, 3029-3032,
1060 <https://doi.org/10.1029/2000GL011599>, 2000.
- 1061 Stanley, W. R., Kaye, P. H., Foot, V. E., Barrington, S. J., Gallagher, M., and Gabey, A.: Continuous
1062 bioaerosol monitoring in a tropical environment using a UV fluorescence particle spectrometer,
1063 *Atmos. Sci. Lett.*, 12, 195–199, doi:10.1002/asl.310, 2011.
- 1064 Stein, A. F., Draxler, R. R., Rolph, G. D., Stunder, B. J. B., Cohen, M. D., and Ngan, F.: NOAA's
1065 hysplit atmospheric transport and dispersion modeling system, *Bull Am Meteorol Soc*, 96 (12), 2059–
1066 2077, <https://doi.org/10.1175/BAMS-D-14-00110.1>, 2015.
- 1067 Toprak, E. and Schnaiter, M.: Fluorescent biological aerosol particles measured with the Waveband
1068 Integrated Bioaerosol Sensor WIBS-4: laboratory tests combined with a one year field study, *Atmos.*
1069 *Chem. Phys.*, 13, 225–243, <https://doi.org/10.5194/acp13-225-2013>, 2013.
- 1070 Visez, N., Ivanovsky, A., Roose, A., Gosselin, S., Sénéchal, H., Poncet, P., and Choël, M.:
1071 Atmospheric particulate matter adhesion onto pollen: a review, *Aerobiologia (Bologna)*, 36, 49-62,
1072 <https://doi.org/10.1007/s10453-019-09616-9>, 2020.
- 1073 Wargenau, A., Fleißner, A., Bolten, C. J., Rohde, M., Kampen, I., and Kwade, A.: On the origin of
1074 the electrostatic surface potential of *Aspergillus niger* spores in acidic environments, *Res Microbiol*,
1075 162 (10), 1011-1017, <https://doi.org/10.1016/j.resmic.2011.07.006>, 2011.
- 1076 Woo, C., An, C., Xu, S., Yi, S. M., and Yamamoto, N.: Taxonomic diversity of fungi deposited from
1077 the atmosphere, *ISME Journal*, 12, 2051–2060, <https://doi.org/10.1038/s41396-018-0160-7>, 2018.
- 1078 Wu, P. C., Tsai, J. C., Li, F. C., Lung, S. C., and Su, H. J.: Increased levels of ambient fungal spores
1079 in Taiwan are associated with dust events from China, *Atmos Environ*, 38, 4879-4886,
1080 <https://doi.org/10.1016/j.atmosenv.2004.05.039>, 2004.
- 1081 Yu, H., Chin, M., Bian, H., Yuan, T., Prospero, J. M., Omar, A. H., Remer, L. A., Winker, D. M.,
1082 Yang, Y., and Zhang, Z.: Quantification of trans-Atlantic dust transport from seven-year (2007–
1083 2013) record of CALIPSO lidar measurements, *Remote Sens. Environ.*, 159, 232–249,
1084 <https://doi.org/10.1016/j.rse.2014.12.010>, 2015.



1085 Yu, H., Tan, Q., Zhou, L., Zhou, Y., Bian, H., Chin, M., Ryder, C. L., Levy, R. C., Pradhan, Y., Shi,
1086 Y., Song, Q., Zhang, Z., Colarco, P. R., Kim, D., Remer, L. A., Yuan, T., Mayol-Bracero, O., and
1087 Holben, B. N.: Observation and modeling of the historic “Godzilla” African dust intrusion into the
1088 Caribbean Basin and the southern US in June 2020, *Atmos. Chem. Phys.*, 21, 12359–12383,
1089 <https://doi.org/10.5194/acp-21-12359-2021>, 2021.

1090